

Broad-band ambient noise surface wave tomography across the United States

G. D. Bensen

Center for Imaging the Earth's Interior, Department of Physics, University of Colorado at Boulder, Boulder, Colorado USA

M. H. Ritzwoller

Center for Imaging the Earth's Interior, Department of Physics, University of Colorado at Boulder, Boulder, Colorado USA

N. M. Shapiro

Laboratoire de Sismologie, CNRS, IGP, Paris, France

Abstract.

This study presents surface wave dispersion maps across the contiguous United States determined using seismic ambient noise. Two years of ambient noise data are used from March 2003 through February 2005 observed at 203 broad-band seismic stations in the US, southern Canada, and northern Mexico. Cross-correlations are computed between all station-pairs to produce empirical Green functions. At most azimuths across the US, coherent Rayleigh wave signals exist in the empirical Green functions implying that ambient noise in the frequency band of this study (5 - 100 s period) is sufficiently isotropically distributed in azimuth to yield largely unbiased dispersion measurements. Rayleigh and Love wave group and phase velocity curves are measured together with associated uncertainties determined from the temporal variability of the measurements. A sufficient number of measurements (>2000) is obtained between 8 and 25 s period for Love waves and 8 and 70 s period for Rayleigh waves to produce tomographic dispersion maps. Both phase and group velocity maps are presented in these period bands. Resolution is estimated to be better than 100 km across much of the US from 8 - 40 s period for Rayleigh waves and 8 - 20 s period for Love waves, which is unprecedented in a study at this spatial scale. At longer and shorter periods, resolution degrades as the number of coherent signals diminishes. The dispersion maps agree well with each other and with known geological and tectonic features and, in addition, provide new information about structures in the crust and uppermost mantle beneath much of the US.

1. Introduction

The purpose of this study is to produce surface wave dispersion maps across the contiguous United States using ambient noise tomography. We present Rayleigh and Love wave group and phase speed maps and assess their resolution and reliability. These maps display higher resolution and extend to shorter periods than previous surface wave maps that have been produced across the United States using traditional teleseismic surface wave tomography methods. The maps presented form the basis for an inversion to produce a higher resolution 3-D model of V_s in the crust and uppermost mantle, but this inversion is beyond the scope of the present paper.

Surface wave empirical Green functions (EGFs) can be determined from cross-correlations between long time sequences of ambient noise observed at different stations. The terms noise correlation function and EGF are sometimes used interchangeably but they differ by an additive phase factor (e.g., *Lin et al.* [2007a]). Investigations of surface wave EGFs have grown rapidly in the last several years. The feasibility of the method was first established by experimental (e.g., *Weaver and Lobkis*

49 [2001], *Lobkis and Weaver* [2001], *Derode et al.* [2003],
50 *Larose et al.* [2005]) and theoretical (e.g., *Sniieder* [2004],
51 *Wapenaar* [2004]) evidence. *Shapiro and Campillo* [2004]
52 demonstrated that the Rayleigh wave EGFs estimated
53 from ambient noise possess dispersion characteristics sim-
54 ilar to earthquake derived measurements and model pre-
55 dictions. The dispersion characteristics of surface wave
56 EGFs derived from ambient noise have been measured
57 and inverted to produce dispersion tomography maps
58 in several geographical settings, such as Southern Cal-
59 ifornia (*Shapiro et al.* [2005]; *Sabra et al.* [2005]), the
60 western US (*Moschetti et al.* [2007]; *Lin et al.* [2007a]),
61 Europe (*Yang et al.* [2007]), Tibet (*Yao et al.* [2006]),
62 New Zealand (*Lin et al.* [2007b]), Korea (*Cho et al.*
63 [2007]), Spain (*Villaseñor et al.* [2007]) and elsewhere.
64 Most of these studies focused on Rayleigh wave group
65 speed measurements obtained at periods below about 20
66 s. *Campillo and Paul* [2003] showed that Love wave sig-
67 nals can emerge from cross-correlations of seismic coda
68 and *Gerstoft et al.* [2006] also noticed several signals on
69 transverse-transverse cross-correlations of ambient noise.
70 These studies did not, however, demonstrate the consis-
71 tent recovery of Love wave signals from ambient noise.
72 Although *Yao et al.* [2006] showed phase speed results,
73 questions about the details of phase speed measurement
74 remained. *Lin et al.* [2007a] placed both phase speed
75 and Love wave measurements on a firm foundation and
76 showed that Love waves are readily observed using ambi-
77 ent noise. We follow their methodology to present phase
78 velocity and Love wave maps here in addition to group ve-
79 locity and Rayleigh wave maps. We apply ambient noise
80 tomography on a geographical scale much larger than all
81 previous studies. The larger spatial scale also allows us
82 to extend the results to longer periods than in previous
83 studies.

84 All of the results presented here are based on the data
85 processing scheme described by *Bensen et al.* [2007]. This
86 method is designed to minimize the negative effects that
87 result from a number of phenomena, such as earthquakes,
88 temporally localized incoherent noise sources, and data
89 irregularities. It also is designed to obtain dispersion
90 measurements to longer periods and along longer inter-
91 station paths than in previous studies, and, thus, in-
92 creases the band-width and the geographical size of the
93 study region.

94 Previous surface wave tomography across the North
95 American continent was based on teleseismic earthquake
96 measurements. Several of these studies involved measure-
97 ments obtained exclusively across North America (e.g.,
98 *Alsina et al.* [1996]; *Godey et al.* [2003]; *van der Lee*
99 *and Nolet* [1997]) whereas others involved data obtained
100 globally (e.g., *Trampert and Woodhouse* [1996]; *Ekström*
101 *et al.* [1997]; *Ritzwoller et al.* [2002]). Ambient noise to-
102 mography possesses complementary strengths and weak-
103 nesses to traditional earthquake tomography. Single-
104 station earthquake tomography benefits from the very
105 high signal-to-noise ratio of teleseismic surface waves and
106 the dispersion measurements extend to very long periods
107 (>100 s) which results in constraints on deep upper man-
108 tle structures. Several characteristics limit the power of
109 traditional earthquake tomography for regional to conti-
110 nental scale studies, however. First, teleseismic propa-
111 gation paths make short period (< 20 s) measurements
112 difficult to obtain in aseismic regions due to the scatter-
113 ing and attenuation that occur as distant waves propa-
114 gate. This is unfortunate because short period mea-
115 surements are needed to resolve crustal structures. This
116 is particularly disadvantageous across the US, which ex-
117 hibits a low level of seismicity in most regions. Second,

118 the long paths also result in broad lateral sensitivity ker-
119 nels which limits resolution to hundreds of kilometers.
120 Third, dispersion measurements from earthquakes typi-
121 cally have unknown uncertainties, unless measures such
122 as cluster analysis from recurring events are employed
123 (*Ritzwoller and Levshin* [1998]); such cluster analysis is
124 still limited to a subset of paths. Finally, uncertainties in
125 source location and depth manifest themselves in uncer-
126 tainties in the “initial phase” of the measurement, which
127 imparts an ambiguity to phase and group speeds mea-
128 sured from earthquakes. Some of these differences can
129 be overcome by two-station phase velocity measurements
130 (*Tanimoto and Sheldrake* [2002]) but advantages of the
131 ambient noise technique for regional to continental scale
132 studies remain.

133 Although the EGFs obtained by cross-correlating
134 long time-series between pairs of stations demonstrate a
135 smaller signal-to-noise ratio than large earthquakes and
136 the resulting ambient noise dispersion measurements typi-
137 cally are limited to periods well below 100 s, ambient
138 noise tomography improves on each of the shortcomings
139 of traditional earthquake tomography. First, ambient
140 noise EGFs provide dispersion maps to periods down to
141 ~ 6 s (and lower in some places with exceptionally dense
142 station spacing), potentially with much better lateral res-
143 olution, particularly in the context of continental arrays
144 of seismometers in which path density and azimuthal cov-
145 erage can be very high. Second, one can estimate uncer-
146 tainties from the repeatability of ambient noise measure-
147 ments (e.g., *Bensen et al.* [2007]). Third, the station lo-
148 cations and the “initial phase” of the EGFs are both well
149 known (*Lin et al.* [2007a]), so the measurements tend to
150 be both more precise and more easily interpreted than
151 earthquake signals.

152 Ambient noise tomography, therefore, provides a sig-
153 nificant innovation in seismic methodology that is now
154 yielding new information about the Earth with reso-
155 lutions near the inter-station spacing. The currently
156 developing Transportable Array component of Earth-
157 Scope/USArray is being deployed on a rectangular grid
158 and is now being used across the western US for ambient
159 noise tomography by *Moschetti et al.* [2007]. Its traverse
160 across the United States will not complete until the year
161 2014, however.

162 This paper is one of the first continental scale ap-
163 plications of ambient noise tomography and is based
164 on 203 permanent and temporary broad-band stations
165 throughout the contiguous US and in southern Canada
166 and northern Mexico (Fig. 1a). Rayleigh wave tomog-
167 raphy maps are created from 8 to 70 s period and Love
168 wave maps from 8 to 25 s period. We present a subset of
169 these maps. These maps provide new information about
170 the crust and mantle beneath the United States, show
171 that the technique is not limited to short periods or re-
172 gional scales, and add further credibility to ambient noise
173 surface wave tomography.

2. Data Processing

174 We follow the method described in detail by *Bensen*
175 *et al.* [2007] for data processing from observations of am-
176 bient seismic noise to the production of group speed mea-
177 surements. Phase speed measurements and Love wave
178 data processing follow the procedure of *Lin et al.* [2007a].
179 We briefly review here the data processing procedure and
180 discuss the repeatability of the dispersion measurements
181 as well as the way in which signal-to-noise ratio (SNR)
182 varies with period and region. In later sections, we dis-
183 cuss how measurements from almost 20,000 inter-station

184 paths are selected to be used for tomographic inversion to
185 estimate group and phase speed dispersion maps (*Barmin*
186 *et al.* [2001]) ranging from 8 to 70 s period for Rayleigh
187 waves and 8 to 25 s period for Love waves.

188 We processed all available vertical and horizontal com-
189 ponent broad-band seismic data from the 203 stations
190 (Fig. 1a) that are available from the IRIS DMC and the
191 Canadian National Seismic Network (CNSN) for the 24-
192 month period from March 2003 through February 2005.
193 Although the data come from this 24-month window,
194 most time-series are shorter than 24-months because of
195 station down time or installation during this period.
196 Time-series lengths are referred to in terms of the time
197 window from which the waveforms derived, but actual
198 time-series lengths vary within the same time window.
199 Station locations are identified in Figure 1a. Station cov-
200 erage in the west and parts of the eastern mid-west is
201 good, but the north-central US and the near-coastal east-
202 ern US are poorly covered. As seen later, this has ram-
203 ifications for resolution. The azimuthal distribution of
204 inter-station paths is shown in Figure 1b. This includes
205 both inter-station azimuth and back-azimuth, presented
206 as the number of paths falling into each 10° azimuth
207 bin. Large numbers at a particular azimuth (or back-
208 azimuth, both are included) correspond to the dominant
209 inter-station directions. For example, in the eastern and
210 central US, stations are oriented dominantly to pick up
211 waves traveling to the north-east or the west. Concentra-
212 tions of stations, such as in California, tend to produce
213 large numbers of inter-station directions in a narrow az-
214 imuthal range. The diagrams are not azimuthally sym-
215 metric because azimuth and back-azimuth are not exactly
216 180° -complements. Figure 1b dominantly reflects the ge-
217 ometry of the seismic network used. Later in the paper,
218 we discuss the directions of propagation of the strongest
219 signals and reference them to the azimuthal distribution
220 of inter-station paths shown in Figure 1b.

221 Data preparation is needed prior to cross-correlation.
222 Starting with instrument response corrected day-long
223 time-series at each station, we first perform time-domain
224 normalization to mitigate the effects of large amplitude
225 events (e.g., earthquakes and instrument glitches). In-
226 itially, researchers favored a 1-bit (or sign bit, or binary)
227 normalization (*Larose et al.* [2004], *Shapiro et al.* [2005]),
228 but *Bensen et al.* [2007] argued for the application of a
229 temporally variable weighting function to retain more of
230 the small amplitude character of the raw data and to al-
231 low for flexibility in defining the amplitude normalization
232 in particular period bands. Here, we define the tempo-
233 ral normalization weights between periods of 15 and 50
234 s, but apply the weights to the unfiltered data. As dis-
235 cussed by *Bensen et al.* [2007], this removes earthquakes
236 from the daily time-series more effectively than defining
237 the temporal normalization on the raw data. The impact
238 is seen most strongly in the quality of the Love wave
239 signals. This procedure is applied to both the vertical
240 and horizontal component data, but the relative ampli-
241 tudes of the two horizontal components must be main-
242 tained. An additional spectral whitening is performed
243 to all of the waveforms for each day to avoid significant
244 spectral imbalance. Again, the same filter must be ap-
245 plied to both horizontal components. Spectral whitening
246 increases the band-width of the automated broad-band
247 dispersion measurements. (*Bensen et al.* [2007]). After
248 temporal and spectral normalization, cross-correlation is
249 performed on day-long time-series for vertical-vertical,
250 east-east, east-north, north-east, and north-north com-
251 ponents. The horizontal components are then rotated to
252 radial-radial (R-R) and transverse-transverse (T-T) ori-

253 entations as defined by the great circle path between the
254 two stations. These daily results are then “stacked” for
255 the desired length of input (e.g. one month, one year,
256 etc.). The Rayleigh wave (Z-Z and R-R) and Love wave
257 (T-T) cross-correlograms yield two-sided (“causal” and
258 “anticausal”) EGFs corresponding to waves propagating
259 in opposite directions between the stations. Both the
260 causal and acausal EGFs are equally valid and can be
261 used as input into the dispersion measurement routine,
262 but may have different spectral content and signal-to-
263 noise ratio characteristics. Both for simplicity and to
264 optimize the band-width of the EGFs, we average the
265 causal and anticausal signals into a single “symmetric
266 signal” from which all dispersion measurements are ob-
267 tained.

268 The frequency dependent group and phase velocities
269 from the Rayleigh and Love wave EGFs are estimated us-
270 ing an automated dispersion measurement routine. Fol-
271 lowing *Levshin et al.* [1972], we performed Frequency-
272 Time Analysis (FTAN) to measure the phase and group
273 velocity dispersion on all recovered signals. The FTAN
274 technique applies a sequence of Gaussian filters at a dis-
275 crete set of periods and measures the group arrival times
276 on the envelope of these filtered signals. Phase velocity
277 is also measured and further details can be found in *Lin*
278 *et al.* [2007a]. We used the 3D model of *Shapiro and Rit-
279 zwoller* [2002] to resolve the 2π phase ambiguity, which is
280 successful in the vast majority of cases. The Rayleigh and
281 Love wave signals apparent on the EGFs are less compli-
282 cated than earthquake signals because the inter-station
283 path lengths are relatively short and the absence of body
284 waves simplifies the signal. This allowed the automation
285 of the dispersion measurements. Selected examples of the
286 symmetric component Rayleigh wave waveforms and the
287 resulting group and phase speed measurements are shown
288 in Figure 2a,b. The broad-band dispersive nature of these
289 waveforms is seen in Figure 2a with longer period energy
290 arriving first. Figure 2b shows the resulting group and
291 phase dispersion curves. The fastest path lies between
292 stations GOGA (Godfrey, GA, USA) and VLDQ (Val
293 d’Or, Quebec, Canada) in the tectonically stable part of
294 eastern North America. The slowest path is between sta-
295 tions DUG (Dugway, AR, USA) and ISA (Isabella, CA,
296 USA) in the tectonically active part of the western US.
297 The other two paths (Camsell Lake, NWT, Canada to
298 Albuquerque, NM, USA; Cathedral Cave, MO, USA to
299 Whiskeytown Dam, CA, USA) have intermediate speeds
300 and propagate through a combination of tectonically de-
301 formed and stable regions.

302 Examination of the Rayleigh and Love wave signals
303 reveals the difference between the speeds and signal
304 strengths. Figure 3 presents examples of Z-Z, R-R, and
305 T-T EGFs in the period range from 5 to 50 s. Figure
306 3a contains the EGFs between stations CCM (Crystal
307 Cave, MO, USA) and RSSD (Black Hills, SD, USA) with
308 an inter-station distance of 1226 km. Rayleigh waves are
309 seen on the vertical-vertical (Z-Z) and radial-radial (R-
310 R) cross-correlograms and arrive at similar times. Love
311 wave signals are seen on the transverse-transverse (T-
312 T) cross-correlograms. The different Rayleigh and Love
313 wave arrival times are clear and are identified with differ-
314 ent velocity windows in the diagram. Figure 3b,c presents
315 record sections for the Z-Z and T-T cross-correlograms
316 from the 13 Global Seismic Network (GSN) stations (*But-
317 ler et al.* [2004]) in the study region. Approximate move-
318 outs of 3.0 and 3.3 km/s for Rayleigh and Love waves are
319 shown in Figures 3b and 3c, respectively.

3. Data Selection

After the EGFs are computed between every station-pair for the Z-Z and T-T components, several selection criteria are applied prior to tomography. The effect of each step of the process in reducing the data set is indicated in Tables 1 and 2.

First, we apply a minimum three wavelength inter-station distance constraint, which is imposed because of measurement instabilities at shorter distances. This criterion significantly reduces the number of measurements at periods above 50 s because stations must be separated by more than 600 km.

Second, we apply a selection criterion based on the period-dependent signal-to-noise ratio (SNR), which is defined as the peak signal in a signal window divided by the root-mean-square (RMS) of the trailing noise, filtered with a specified central period. Average SNR values for the Z-Z, R-R, and T-T EGFs are seen in Figure 4a. A dispersion measurement is retained at a period if the SNR > 15 for the EGF at that period. A lower SNR value is accepted if the measurement variability is small, as will be described below.

Similarities in the patterns of SNR as a function of period for Rayleigh waves on the Z-Z and R-R components are observed in Figure 4a up to 20 s period; although the R-R signal quality is lower. Above 20 s period, the R-R SNR degrades more quickly, however, similar to the trend of the SNR for the T-T cross-correlations. This pattern is consistent with the results of *Lin et al.* [2007a]. Apparently, the SNR degrades at longer periods on horizontal components predominantly due to increasing levels of incoherent local noise, and may not be due to decreasing signal levels. Because the SNR is much higher on the Z-Z than the R-R components and the Z-Z band-width is larger, we only use Rayleigh wave dispersion measurements obtained on the Z-Z EGFs.

Figure 4b,c presents information about the geographical distribution of SNR. The average SNR of all waveforms is shown for Rayleigh (Z-Z) and Love (T-T) wave signals in each of the four regions defined in Figure 1a where both stations lie within the sub-region. SNR in the sub-regions is higher than over the entire data set (Fig. 4a) because path lengths are shorter, on average, by more than a factor of two in the regional data. Rayleigh wave SNR is highest in the south-west region, with SNR in the other regions being lower but similar to each other. Long period SNR, in particular, is considerably higher in the south-west than in other regions. In most regions, the Rayleigh wave curves show double peaks apparently related to the primary and secondary microseism periods of 15 and 7.5 s, respectively.

For Love waves, the highest SNR is in the south-west and north-west regions and the curves display only a single peak near the primary microseismic band, peaking in different regions between 13 and 16 s period. The highest Love wave SNR is in the north-west, unlike the Rayleigh waves which are highest in the south-west region. This implies that the distribution of Rayleigh and Love wave energies differ and they may not be co-generated everywhere. Although Figure 4a shows that below 15 s period Love waves have a higher average SNR than Rayleigh waves, this is true only in the western US. In the central and eastern US, Rayleigh and Love waves below about 15 s have similar SNR values implying similar energy strengths. In all regions, Love wave signals are negligible above about 25 s period. Love wave signals are much stronger in the western US than in the central or eastern US, particularly above about 15 s period. These

387 results indicate clearly that the strongest ambient noise
388 sources are located generally in the western US, although
389 substantial Rayleigh wave signal levels also exist in the
390 central and eastern US. Love waves in the central and
391 eastern US, however, are much weaker above about 15 s.

392 Third, we apply a data selection criterion based on
393 the variability of measurements repeated on temporally
394 segregated subsets of the data. We compiled EGFs for
395 overlapping 6-month input time-series (e.g., June, July,
396 August 2003 plus June, July, August 2004) to obtain
397 12 “seasonal” stacks. We measure the dispersion curves
398 on data from each 6-month (dual 3-month) time win-
399 dow and on the complete 24-month time window. For
400 each station-pair, the standard deviation of the disper-
401 sion measurements is computed at a particular period
402 using data from all of the 6-month time windows in which
403 $\text{SNR} > 10$ at that period. An illustration of this proce-
404 dure appears in Figure 5. Figure 5a shows the Z-Z, R-R,
405 and T-T EGFs used from the 2685 km long path between
406 stations DWPF (Disney Wilderness Preserve, FL, USA)
407 and RSSD (Black Hills, SD, USA). Figure 5b,c,d com-
408 pares the measurements obtained on the 6-month tempo-
409 ral subsets of data with the 24-month group and phase
410 velocity measurements. The error bars indicate the com-
411 puted standard deviations. If fewer than four 6-month
412 time-series satisfy the criterion that $\text{SNR} > 10$, then the
413 standard deviation of the measurement is considered in-
414 determinate and we assign three times the average of the
415 standard deviations taken over all measurements within
416 the data set. The average standard deviation values
417 are shown in Figure 6. Finally, we reject measurements
418 for a particular wave type (Rayleigh/Love, group/phase
419 speed) and period if the estimated standard deviation is
420 greater than 100 m/s, as this indicates an instability in
421 the measurement. The inverse of the standard deviation
422 is used as a weight in the tomographic inversion (e.g.,
423 *Barrin et al.* [2001]).

424 In contrast with Figure 6, Figure 7 contains the mean
425 measurement standard deviation values for each of the
426 four sub-regions defined in Figure 1a. The measure-
427 ments are labeled for Rayleigh and Love wave group and
428 phase measurements. The patterns are similar for all sub-
429 regions. Because dramatic differences between measure-
430 ment uncertainties in different regions are not observed,
431 similar measurement quality is obtained in all regions
432 even though there are differences between the regions in
433 average SNR and, therefore, different numbers of mea-
434 surements in each region. The most stable measurements
435 are Rayleigh wave phase speeds, particularly above about
436 20 s period where phase speed is more robust than group
437 speed. Below 20 s period, the envelope on which group
438 velocity is measured becomes narrower at short periods
439 and increases measurement precision. Thus, the accuracy
440 of the group velocity measurements becomes similar to
441 the phase velocity measurements below 20 s period. Al-
442 though the Love wave phase velocity measurements have
443 favorable standard deviation with increasing period, the
444 number of high quality measurements above 20 s period
445 drops precipitously due to low signal levels. Finally, as a
446 rule-of-thumb, at periods above about 30 s, the standard
447 deviation of Rayleigh wave phase speed measurements is
448 about half that of group speed.

449 Fourth, we apply a final data selection crite-
450 rion based on tomographic residuals. Using the
451 thus far accepted measurements, we create an overly-
452 smoothed tomographic dispersion map for each wave type
453 (Rayleigh/Love, group/phase velocity). Measurements
454 for each wave type with high travel time residuals (three
455 times the root-mean-squared residual value at a given pe-

456 riod and wave type) are removed and the overly smoothed
 457 dispersion map is recreated, becoming the background
 458 dispersion map for a later less damped inversion.

459 The final Rayleigh wave (Z-Z) path retention statistics
 460 for selected periods are shown in Table 1. Similar statis-
 461 tics for Love waves (T-T) at periods of 10, 16 and 25 s
 462 period are shown in Table 2. The number of paths re-
 463 tained at periods above about 70 s for Rayleigh waves and
 464 25 s for Love waves is insufficient for tomography across
 465 the US, but the longer period measurements would be
 466 useful in combination with teleseismic dispersion mea-
 467 surements.

4. Azimuthal distribution of signals

468 The theoretical basis for surface wave dispersion mea-
 469 surements obtained on from EGFs and the subsequent to-
 470 mography assumes that ambient noise is distributed ho-
 471 mogeneously with azimuth (e.g., *Snieder* [2004]). Asym-
 472 metric two-sided EGFs, such as those shown in Figure 3a
 473 and documented copiously elsewhere (e.g., *Stehly et al.*
 474 [2006]), illustrate that the strength and frequency content
 475 of ambient noise vary appreciably with azimuth. This
 476 motivates the question as to whether ambient noise is
 477 well enough distributed in azimuth to return unbiased
 478 dispersion measurements for use in tomography. *Lin*
 479 *et al.* [2007a] present evidence, based on measurements
 480 of the “initial phase” of phase speed measurements from
 481 a three-station method, that in the frequency band they
 482 consider (6 - 40 s period) ambient noise is distributed
 483 sufficiently isotropically so that phase velocity measure-
 484 ments are returned largely unbiased. *Yang and Ritzwoller*
 485 [2007] performed synthetic experiments to quantify the
 486 effect of strongly anisotropic background noise source dis-
 487 tribution. They found that in the presence of low level
 488 homogeneously distributed ambient noise, much stronger
 489 ambient noise in an off-axis direction affects measured
 490 phase velocities by less than 0.5%.

491 *Stehly et al.* [2006] left the precision of group velocity
 492 measurements in doubt after showing strong azimuthal
 493 imbalance of signal strength in the western US. The reli-
 494 ability of group velocity measurements on such EGFs was
 495 tested by *Stehly et al.* [2007] on both the causal and anti-
 496 causal parts of EGFs. They compared measured velocity
 497 from EGFs computed from one-month duration ambient
 498 noise time series to measurements from a baseline Green
 499 function and found that measurement variability was less
 500 than 0.3% and in certain cases less than 0.02%. Even
 501 with a noise distribution shown to be decidedly inhomog-
 502 eneous, there is little effect on the precision of measured
 503 group velocity.

504 According to *Yang and Ritzwoller* [2007], therefore, to
 505 show that the measurements on EGFs used for tomogra-
 506 phy are indeed accurate, we need only show that strong
 507 signals exist in some azimuths. In this assessment, the
 508 distribution of paths dictated by the geometry of the ar-
 509 ray must be borne in mind. Consequently, all results are
 510 taken relative to the azimuthal distribution of the ob-
 511 serving network presented in Figure 1b. In addition to
 512 solidifying confidence in EGF dispersion measurements,
 513 much can be learned about the character of the ambient
 514 noise environment in North America.

515 Figure 8 presents the azimuthal distribution of high
 516 SNR Rayleigh wave signals at periods of 8, 14, 25 and 40
 517 s. Our measurements are divided into three sub-regions
 518 as defined in Figure 1a, but with the central and eastern
 519 regions combined. Only one station in each station-pair is
 520 required to be in a sub-region. Both azimuth and back-
 521 azimuth are included in the figure. Averaging over all

522 regions and azimuths, at periods of 8, 14, 25, and 40 s the
523 fraction of Rayleigh wave EGFs with a SNR > 10 is 0.38,
524 0.49, 0.54 and 0.38, respectively, and reduces quickly for
525 periods above 40 s. To compute this fraction as a function
526 of azimuth, the number of paths with SNR > 10 in a given
527 20° azimuth bin is divided by the total number of paths
528 in that bin given by Figure 1b. The SNR on both EGF
529 lags is considered separately, and the indicated azimuth is
530 the direction of propagation. We refer to the positive and
531 negative lag contributions as having come from different
532 “paths” for simplicity, but, in fact, the paths are the same
533 and only the azimuths differ.

534 Inspection of Figure 8 reveals that the fraction of rel-
535 atively high SNR paths at a given azimuth is often more
536 homogeneously distributed than the western US results
537 of *Stehly et al.* [2007] or the synthetic results of *Yang and*
538 *Ritzwoller* [2007]. At 14 and 25 s period, in all three re-
539 gions all azimuths have the fraction of paths with SNR
540 > 10 above 20% and, hence, the distribution of useful
541 ambient noise signals sufficient to imply accuracy, even
542 though the highest SNR signals may arrive from only a
543 few principal directions. At 8 s period, the results are
544 not as geographically consistent. In the two western re-
545 gions, the strongest signals are those with noise coming
546 from the west. This agrees with the notion that these re-
547 sults would be dominated by the 7.5 s period secondary
548 microseism. In the east and central regions, however, sig-
549 nals come both from the west and northeast and there are
550 fewer high SNR EGFs. Finally, moving to 40 s period, the
551 overall fraction of high SNR measurements is lower. Rel-
552 ative to this lower level, there are still azimuths where the
553 SNR is higher, perhaps implying dominant noise source
554 directions. The azimuthal pattern above 40 s in each re-
555 gion remains about the same as at 40 s, but the fraction
556 of high SNR observations diminishes rapidly.

557 Similar results are obtained for Love waves, as can
558 be seen in Figure 9. Strong Love wave signals are most
559 isotropic in the primary microseismic band, the center
560 column in Figure 9. In the secondary microseismic band,
561 strong Love waves are less isotropic, particularly in the
562 Central US. Nevertheless, azimuthal coverage sufficiently
563 homogeneous for accurate measurements. Above 20 s pe-
564 riod, however, the number of large amplitude signals di-
565 minishes rapidly, particularly in the east. In the west,
566 some large amplitude signals exist, but emerge domi-
567 nantly from the northwest and southeast directions. Sig-
568 nal amplitude above 20 s period is insufficient for tomog-
569 raphy on a large scale.

570 A possible concern with interpreting these plots is
571 the potential for bias by signals from short inter-station
572 paths. In Figure 10 we show an example of the distance
573 and azimuth distribution of signals with SNR > 10 in
574 the central-east region at 25 s period. Long distance high
575 SNR arrivals are seen, and the distribution is mainly con-
576 trolled by the array configuration. Such array induced
577 limitations are observed in the other regions as well.

578 In conclusion, therefore, at all periods studied, in all
579 regions and most azimuths, a useful level of coherent
580 Rayleigh wave signals exist in ambient noise. Stronger
581 azimuthal imbalance is most pronounced at periods be-
582 low 10 s, where most of the Rayleigh wave energy is com-
583 ing generally from the west. Coherent Love wave sig-
584 nals exist at most azimuths from 8 s to 20 s period, but
585 at longer periods both the azimuthal coverage and the
586 strength of Love waves diminish rapidly. These observa-
587 tions, combined with recent theoretical and experimental
588 work, provide another item in a growing list of evidence
589 indicating that ambient noise in this frequency band is
590 distributed in azimuth in such a way to yield largely un-

591 biased dispersion measurements.

5. Tomography

592 An extensive discussion of the tomography procedure
 593 was presented by *Barmin et al.* [2001]. We follow their
 594 discussion to provide a basic introduction to the over-
 595 all procedure and define some needed terms. The tomo-
 596 graphic inversion is a 2-D ray theoretical method, similar
 597 to a Gaussian beam technique and assumes wave propa-
 598 gation along a great circle but with “fat” rays. Starting
 599 with observed travel times we estimate a model \mathbf{m} (2-D
 600 distribution of surface wave slowness) by minimizing the
 601 penalty functional:

$$(\mathbf{G}(\mathbf{m}) - \mathbf{d})^T \mathbf{C}^{-1} (\mathbf{G}(\mathbf{m}) - \mathbf{d}) + \alpha^2 \|\mathbf{F}(\mathbf{m})\|^2 + \beta^2 \|\mathbf{H}(\mathbf{m})\|^2, \quad (1)$$

603 where \mathbf{G} is the forward operator computing travel times
 604 from a model, \mathbf{d} is the data vector of measured surface
 605 wave travel times, and \mathbf{C} is the data covariance matrix
 606 assumed here to be diagonal and composed of the square
 607 of the measurement standard deviations. $\mathbf{F}(\mathbf{m})$ is the
 608 spatial smoothing function where

$$\mathbf{F}(\mathbf{m}) = \mathbf{m}(\mathbf{r}) - \int_S S(\mathbf{r}, \mathbf{r}') \mathbf{m}(\mathbf{r}') d\mathbf{r}', \quad (2)$$

610 and

$$S(\mathbf{r}, \mathbf{r}') = K_0 \exp\left(-\frac{|\mathbf{r} - \mathbf{r}'|^2}{2\sigma^2}\right) \quad (3)$$

612 where

$$\int_S S(\mathbf{r}, \mathbf{r}') d\mathbf{r}' = 1, \quad (4)$$

614 and \mathbf{r} is the target location and \mathbf{r}' is an arbitrary lo-
 615 cation. The functional \mathbf{H} penalizes the model based on
 616 path density and azimuthal distribution.

617 The contributions of \mathbf{H} and \mathbf{F} are controlled by the
 618 damping parameters α and β in equation (1) while spatial
 619 smoothing (related to the fatness of the rays) is controlled
 620 by adjusting σ in equation (3). These three parameters
 621 (α , β and σ) are user controlled variables that are deter-
 622 mined through trial and error optimization.

623 The resulting spatial resolution is found at each point
 624 by fitting a 2-D Gaussian function to the resolution ma-
 625 trix (map) defined as follows:

$$A \exp\left(-\frac{|\mathbf{r}|^2}{2\gamma^2}\right) \quad (5)$$

627 where \mathbf{r} here denotes the distance from the target point.
 628 The fit parameter is the standard deviation of the Gaus-
 629 sian function, γ , which quantifies the spatial size of the
 630 features that can be determined reliably in the tomo-
 631 graphic maps. In this paper, we report 2γ as the res-
 632 olution, the full-width of the resolution kernel at each
 633 point. Figure 11a shows the resolution map for the 10 s
 634 Rayleigh wave group speed. The corresponding ray cov-
 635 erage is shown in Figure 11b. The more densely instru-
 636 mented regions, such as southern California and near the
 637 New Madrid seismic zone in the central United States,
 638 have resolution <70 km, which is better than the inter-

639 station spacing in these regions. Across most of the US,
640 resolution averages about 100 km for Rayleigh waves up
641 to 40 s period and then degrades to 200 km at 70 s period.
642 For Love waves, resolution averages about 130 km below
643 20 s period, but then rapidly degrades at longer periods
644 so that at 20 s the average resolution is about 200 km.
645 The rapid degradation of average resolution in the US
646 for Love waves is due to the loss of Loves wave signals
647 in the eastern US, which sets on at about 15 s period,
648 as discussed above. Regions with resolution worse than
649 1000 km are indicated on the tomographic maps in grey
650 and, in addition, to outline the high resolution regions
651 we plot the 200 km resolution contours.

652 We use ray theory as the basis for tomography in this
653 study, albeit with “fat rays” given by the correlation
654 length parameter σ . In recent years, surface wave studies
655 have increasingly moved toward diffraction tomography
656 using spatially extended finite-frequency sensitivity ker-
657 nels based on the Born/Rytov approximation (*Spetzler*
658 *et al.* [2002]; *Ritzwoller et al.* [2002]; *Yoshizawa and Ken-*
659 *nett* [2002]; and many others). *Ritzwoller et al.* [2002]
660 showed that ray theory with fat rays produces similar
661 structure to diffraction tomography in continental regions
662 at periods below 50 s and the similarities strengthen as
663 path lengths decrease. *Yoshizawa and Kennett* [2002]
664 argued that the spatial extent of sensitivity kernels is
665 effectively much less than given by the Born/Rytov the-
666 ory, being confined to a relatively narrow “zone of influ-
667 ence” near the classical ray. They conclude, therefore,
668 that in many applications, off-great-circle propagation
669 may provide a more important deviation from straight-
670 ray theory than finite frequency effects. *Ritzwoller and*
671 *Levshin* [1998] show that off-great-circle propagation can
672 be largely ignored at periods above about 30 s for paths
673 with distances less than 5000 km, except in extreme cases.
674 From a practical perspective then, these arguments sup-
675 port the contention that ray-theory with ad-hoc fat rays
676 can adequately represent wave propagation for most of
677 the path lengths and most of the period range under
678 consideration here. A caveat is for relatively long paths
679 (>1000 km) at short periods (<20 s), in which case off-
680 great-circle effects may become important. Off-great-
681 circle effects will be largest near structural gradients,
682 but are mitigated by observations made on orthogonal
683 paths. In our study region, where structural gradients
684 are largest, azimuthal path coverage tends to be quite
685 good. These considerations lead us to conclude that ray
686 theory with fat-rays is sufficient to produce meaningful
687 dispersion maps and that uncertainties in the maps pro-
688 duced by the arbitrariness of the choice of the damping
689 parameters are probably larger than errors induced by
690 the simplified theory. Nevertheless, future work is needed
691 to test this assertion quantitatively. We anticipate only
692 subtle changes to the dispersion maps.

6. Results

693 In this section we present examples of the tomographic
694 maps with the particular purpose of establishing their
695 credibility and limitations. In the next section, we qual-
696 itatively discuss some of the structural features that ap-
697 pear in the maps.

698 The tomography method, described in the preceding
699 section, is applied to the final set of accepted measure-
700 ments to produce dispersion maps from 8 to 70 s period
701 for Rayleigh waves and 8 to 25 s period for Love waves. In
702 this period range more than 2000 measurements exist for
703 all wave types. The method is applied on a $0.5^\circ \times 0.5^\circ$
704 geographical grid across the study region. Examples of the

705 resulting dispersion maps are presented in Figures 12 - 15.
 706 In all maps, the 200 km resolution contour is shown with
 707 a thick black or grey contour and the grey regions are
 708 those areas on the continent that have indeterminate ve-
 709 locities. The damping parameters α and β in equation (1)
 710 which control the strength of the smoothness constraint
 711 and the tendency of the inversion to stay at the input
 712 model are determined subjectively to supply acceptable
 713 fit to the data, while retaining the coherence of large-
 714 scale structures and controlling the tendency of streaks
 715 and stripes to contaminate the maps. The smoothing or
 716 correlation length parameter, σ , is chosen to be 125 km
 717 at periods below 25 s and 150 km at longer periods. As
 718 with any tomographic inversion, the resulting maps are
 719 not unique but the features that we discuss below are
 720 common to any reasonable choice of the damping and
 721 smoothness parameters.

722 Discussion of the tomographic maps is guided by the
 723 vertical V_s sensitivity kernels shown in Figure 16. At a
 724 given period, phase velocity measurements tend to sense
 725 deeper structures than group velocity measurements and
 726 Rayleigh waves sense deeper than Love waves. Thus, at
 727 any period the Rayleigh wave phase velocities will have
 728 the deepest sensitivity and the Love wave group velocities
 729 will be most sensitive to shallow structures.

730 Figures 12 and 13 show Rayleigh and Love wave group
 731 and phase speed maps at 10 and 20 s period, respectively.
 732 Sedimentary thickness contours are over-plotted in Fig-
 733 ure 12 and will be discussed further in the next section.
 734 The 10 s maps are all similar to one another, with much
 735 lower speeds in the western than the eastern US. The sim-
 736 ilarity of the maps is expected because these wave types
 737 are all predominantly sensitive to crustal structures, no-
 738 tably the existence of sediments. Thus, the principal fea-
 739 tures on these maps are slow anomalies correlated with
 740 sedimentary basins, as discussed later. The 20 s maps
 741 are also similar to one another, with the exception of the
 742 Rayleigh phase velocity map. The 20 s Rayleigh group
 743 velocity and Love wave group and phase velocity maps
 744 are more similar to the 10 s maps than the 20 s phase
 745 velocity map. This is because, like the 10 s results, these
 746 maps are mostly sensitive to the wave speeds within the
 747 crust. This similarity between these maps lends credibil-
 748 ity to the tomographic results at short periods.

749 As Figure 16b shows, the 20 s Rayleigh wave phase
 750 velocity map has a substantial sensitivity to the mantle
 751 and is better correlated with intermediate period maps.
 752 Examples of results at intermediate periods are shown in
 753 Figure 14, which presents a comparison between the 25
 754 s Rayleigh wave phase speed and the 40 s Rayleigh wave
 755 group speed maps. Figure 16c also shows that these two
 756 wave types have similar vertical sensitivity kernels, both
 757 waves being predominantly sensitive to shear velocities
 758 in the uppermost mantle. The measurements, however,
 759 are entirely different. We view the similarity between
 760 these maps, therefore, as a qualitative confirmation of
 761 the procedure at intermediate periods.

762 The longest period map presented here is the 60 s
 763 Rayleigh wave phase speed map shown in Figure 15a.
 764 This map possesses considerable sensitivity to the upper
 765 mantle to a depth of about 150 km. It is compared to
 766 the map for the same wave type computed from the 3-D
 767 model of *Shapiro and Ritzwoller* [2002] shown in Figure
 768 15b. At large scales, the maps are similar both in the dis-
 769 tribution and absolute value of velocity. Considering all
 770 points of 15 with resolution better than 1000 km, the 60 s
 771 phase speed map derived from ambient noise is about 2%
 772 faster than the results of *Shapiro and Ritzwoller* [2002].
 773 Omitting points near the coast where resolution is lower,

774 this difference decreases to less than 1% faster. A more
775 damped version of the ambient noise map agrees even
776 better with the model prediction.

777 The fit of individual dispersion measurements to the
778 tomographic maps reveals more about the quality of the
779 data. The first type of information is the variance re-
780 duction relative to a homogeneous model, which here is
781 taken to be the average of the measurements at each wave
782 type and period. Figure 17a shows the variance reduc-
783 tion for the Rayleigh and Love wave group and phase
784 speed maps from 10 to 90 s period. (Rayleigh wave maps
785 above 70 s period and Love wave maps above 25 s peri-
786 od are created in order to extend these statistics to the
787 longer periods.) The largest variance reductions are for
788 the Rayleigh wave phase velocity measurements, which
789 are above 90% for the entire period range. Below 20
790 s period, a similar variance reduction is achieved by the
791 Rayleigh wave group speed maps. Love wave variance re-
792 duction is mostly lower. Love wave results above about
793 25 s period are of little meaning because the number of
794 measurements is so low. For all wave types, the mean
795 path length is about the same (around 1800 km) for all
796 periods. The variance reduction reflects the rms residual
797 level after tomography, which is plotted both in time and
798 velocity in Figure 17b,c. Rayleigh wave rms phase travel
799 time residuals are between 2 and 3 s across the whole
800 band, and travel time residuals for the other wave types
801 are mostly between 6 and 10 s. In particular, Rayleigh
802 wave group travel times residuals are 2 - 3 times larger
803 than the anomalies for Rayleigh phase, consistent with
804 the standard deviation of the phase velocity measurement
805 being about half that for group velocity.

7. Discussion

806 Detailed interpretation of surface wave dispersion
807 maps is difficult because their sensitivity kernels are ex-
808 tended in depth and the group velocity kernels they ac-
809 tually change sign. We present a qualitative discussion of
810 Figures 12 - 15 here, but a more rigorous interpretation
811 must await a 3-D inversion for Vs structures in the crust
812 and uppermost mantle, which is beyond the scope of this
813 paper. Many of the features of the maps in Figures 12 -
814 15 are not surprising, as they represent structures on a
815 larger spatial scale similar to those revealed by the ear-
816 lier work of *Shapiro et al.* [2005], *Lin et al.* [2007b], and
817 *Moschetti et al.* [2007] in the western US. The details of
818 the maps and how they vary with period, particularly at
819 longer periods and in the eastern US, are entirely new,
820 however.

821 Overall, the most prominent anomaly on all maps is
822 the continental-scale east-west dichotomy between the
823 tectonically active western US and the cratonic eastern
824 US. This dichotomy is observed at all periods, so it ex-
825 presses both crustal and mantle structures, although its
826 contribution tends to grow with increasing period, at
827 least in a relative sense. In terms of smaller scale re-
828 gional structures, lateral crustal velocity anomalies that
829 manifest themselves in surface wave dispersion maps
830 are largely compositional in origin, whereas the man-
831 tle anomalies are probably predominantly thermal, al-
832 though volatile content may also contribute to low ve-
833 locity anomalies in both the crust and mantle. The
834 most significant shallow crustal lateral velocity anomalies
835 are due to velocity differences between the sedimentary
836 basins and surrounding crystalline rocks, which are more
837 significant than velocity variations within the crystalline
838 crust. Large-scale anomalies in the uppermost mantle
839 correspond to variations in lithospheric structure and

840 thickness, predominantly reflecting differences between
841 the thin tectonic lithosphere of the western US and the
842 thicker cratonic lithosphere of the eastern and central US.
843 Regional scale anomalies reflect variations in the thermal
844 state of the uppermost mantle and crustal thickness.

845 Below 20 s period (i.e., Figures 12 and 13), the dis-
846 persion maps dominantly reflect low velocity anomalies
847 caused by sedimentary basins. The sediment model of
848 (*Laske and Masters [1997]*) is shown in Figure 18 for com-
849 parison, with several principal structural units identified.
850 Isopach contours are superimposed in Figure 12 with a
851 1 km interval for reference. The 10 s period maps re-
852 veal low velocity anomalies associated with sediments in
853 the Great Valley (CV) of central California as well as the
854 Salton Trough/Imperial Valley of southern California ex-
855 tending down into the Gulf of California (GC). Low veloc-
856 ity anomalies are also coincident with the Anadarko (AB)
857 basin in Texas/Oklahoma and the Permian Basin (PB)
858 in west Texas. The deep sediments in the Gulf of Mexico
859 (GOM) produce the largest low velocity features. Other
860 basins such as the Wyoming-Utah-Idaho thrust belt (TB)
861 extending north to the Williston basin (WB) also are ap-
862 parent. This feature is seen best on the Love wave group
863 speed map (Figure 12c) which has the shallowest sensi-
864 tivity (see Figure 16a). Rayleigh wave phase speed on
865 the other hand has deeper sensitivity and the Williston
866 basin is only vaguely seen as a relative low velocity fea-
867 ture in Figure 12b. The Appalachian Basin (ApB) also
868 appears as a relative slow anomaly in all maps, although
869 it is less pronounced due to the generally higher wave
870 speeds and older (hence faster) sediments in the eastern
871 US. The Michigan Basin (MB) is not observed, probably
872 because of the lower resolution in the central US than in
873 west where station coverage is better.

874 Low wave speeds observed in the 10 s maps for the
875 Basin and Range (BR) and Pacific Northwest (PNW)
876 are interesting considering the lack of deep sedimentary
877 basins. These anomalies, therefore, are probably due to
878 thermal or compositional anomalies within the crystalline
879 crust rather than in the sediment overburden.

880 Many of the features of the 10 s maps in Figure 12 are
881 also seen in the 20 s maps of Figure 13. The range of
882 depth sensitivities for the 20 s dispersion maps is broad
883 (Figure 16), however, and the 20 s Rayleigh wave phase
884 speed map (Figure 13b) is more like longer period maps.
885 In addition, the shallower and older basins are not ob-
886 served and the Sierra Nevada (SN) high velocity anomaly
887 emerges more clearly at 20 s than at 10 s period. High
888 speed anomalies are observed in the Gulf of California,
889 in contrast to the 10 s maps, due to thin oceanic crust.

890 At intermediate periods (25 - 40 s), waves are primar-
891 ily sensitive to depths between 25 and 70 km; namely,
892 the deep crust (in places), crustal thickness, and the up-
893 permost mantle. The Rayleigh wave 25 s phase speed
894 map and the 40 s group speed map have maximum sensi-
895 tivities at about 50 km depth and similar kernels, as
896 Figure 16 illustrates. Thick crust tends to appear as
897 slow velocity anomalies and thin crust as fast anom-
898 alies on the maps. The anomalies on the maps in Figure
899 14 are similar to one another, with a few exceptions. The
900 low velocity anomalies through the Rocky Mountain Re-
901 gion (RM, Colorado, Wyoming, eastern Utah, southern
902 Idaho) and the Appalachian Mountains (ApM, northern
903 Alabama to western Pennsylvania) are probably the most
904 prominent low velocity features and they reflect thicker
905 crust than average. To focus on this further, the box
906 drawn in the western panel of Figure 14b is shown in
907 greater detail in Figure 19. Over-plotted in this figure is
908 the depth to Moho model of *Seber et al. [1997]* with a 2.5

909 km contour interval. In general, areas with thicker crust
910 in Nevada, Utah, Idaho, Wyoming, and Colorado have
911 slower wave speeds, as expected. The bone-shaped high
912 velocity anomaly of eastern Nevada corresponds to thin-
913 ner crust beneath the Great Basin. East of Colorado,
914 however, crustal velocities are higher due to the east-
915 west tectonic dichotomy of the US and the lithosphere
916 thickens beneath cratonic North America, which partially
917 compensates for the low velocities that result from the
918 thick crust. For this reason, the low velocities beneath
919 the Rocky Mountain region do not extend into the central
920 US. Nevertheless, the low velocities of the Colorado
921 Plateau probably also reflect elevated crustal tempera-
922 tures in addition to thicker crust. High velocity anomalies
923 along the coasts, in southern Arizona, and northwestern
924 Mexico reflect thinner crust in these regions.

925 Not all low velocity anomalies at intermediate periods
926 have their origin in thicker crust. In the Pacific North-
927 west (PNW) states of northern California, Oregon, and
928 Washington, slow anomalies are probably caused by a
929 warm, volatilized mantle wedge overlying the subducting
930 Juan de Fuca and Gorda plates. These low velocities are
931 not seen south of the Mendocino triple junction where
932 the subducting slab is no longer present in the shallow
933 mantle. Perhaps surprisingly, the effect of the Anadarko
934 Basin (AB) in western Oklahoma persists to these pe-
935 riods. Figure 16c illustrates that even at intermediate
936 periods very shallow structures will have a contribution
937 to surface wave speeds.

938 Some features differ between the 25 s group speed and
939 the 40 s phase speed maps, however. We note two. First,
940 the 40 s phase speed map has low velocities extending east
941 into Nebraska and South Dakota, whereas these features
942 are more subdued on the 25 s group speed map. Second,
943 the 25 s group speed map has a high velocity anomaly in
944 Michigan which is largely missing on the 40 s phase speed
945 map, although Michigan does appear as a relatively fast
946 feature in this map. These discrepancies are small, and
947 overall the maps agree quite well.

948 Moving to deeper mantle sensitivity, Figure 15a shows
949 the phase speed map at 60 s period. This wave is most
950 sensitive to depths from 50 to 150 km and reveals fea-
951 tures of mantle structure and lithospheric thickness, in
952 contrast to the shallower sensitivity of maps in Figure
953 14. The cold, thick lithosphere beneath the cratonic core
954 of the continent appears clearly as a fast anomaly in the
955 central and eastern US, while the thinner lithosphere in
956 the western United States appears as low velocities over
957 a large area. The transition between the tectonic and
958 cratonic lithosphere is similar in both maps, but the am-
959 bient noise map reveals more of a stair-step latitudinal
960 structure rather than the more continuous variation with
961 latitude found in the 3-D model prediction. The low-
962 est velocities of the map are in the high lava plains of
963 southeast Oregon and northwest Nevada, which is be-
964 lieved to be the location of the first surface expression of
965 the plume that currently underlies Yellowstone. Yellow-
966 stone itself is below the resolution of the maps presented
967 in this study. However, a low velocity anomaly does
968 appear in the maps derived from ambient noise tomog-
969 raphy based on the Transportable Array component of
970 EarthScope/USArray (*Moschetti et al.* [2007]; *Lin et al.*
971 [2007b]). Very low velocities are also associated with the
972 Sierra Madre Occidental in western Mexico, which is a
973 Cenozoic volcanic arc.

8. Conclusions

974 We computed cross-correlations of long time sequences

975 of ambient seismic noise to produce Rayleigh and Love
976 wave empirical Green functions between pairs of stations
977 across North America. This is the largest spatial scale
978 at which ambient noise tomography has been applied, to
979 date. Cross-correlations were computed using up to two
980 years of ambient noise data recorded from March of 2003
981 to February of 2005 at ~ 200 permanent and temporary
982 stations across the US, southern Canada, and northern
983 Mexico. The period range of this study is from about 5
984 to 100 s. We show that at all periods and most azimuths
985 across the US, coherent Rayleigh wave signals exist in
986 ambient noise. Thus, ambient noise in this frequency
987 band across the US is sufficiently isotropically distributed
988 in azimuth to yield largely unbiased dispersion measure-
989 ments.

990 Rayleigh and Love wave group and phase speed curves
991 were obtained for every inter-station path, and uncer-
992 tainty estimates (standard deviations) were determined
993 from the variability of temporal subsets of the measure-
994 ments. Phase velocity standard deviations are about
995 half the group velocity standard deviations, on average.
996 These uncertainty estimates and the frequency depen-
997 dent signal-to-noise ratios were used to identify the ro-
998 bust dispersion curves, with total numbers changing with
999 period and wave type up to a maximum of about 8500.
1000 Sufficient numbers of measurements (more than 2000) to
1001 perform surface wave tomography were obtained for Love
1002 waves between about 8 and 25 s period and for Rayleigh
1003 waves between about 8 and 70 s period. A subset of
1004 these maps are presented herein. Resolution (defined as
1005 twice the standard deviation of a 2-D Gaussian function
1006 fit to the resolution surface at each point) is estimated
1007 to be better than 100 km across much of the US at most
1008 periods, but it degrades at the longer periods and degen-
1009 erates sharply near the edges of the US, particularly near
1010 coastlines. This resolution is unprecedented in a study
1011 at the spatial scale of this one.

1012 In general, the dispersion maps agree well with each
1013 other and with known geological features and, in addi-
1014 tion, provide new information about structures in the
1015 crust and uppermost mantle beneath much of the US.
1016 Inversion to estimate 3-D Vs structure in the crust and
1017 uppermost mantle and to constrain crustal anisotropy are
1018 natural extensions of this work.

1019 **Acknowledgments.** All of the data used in this research
1020 were downloaded either from the IRIS Data Management Cen-
1021 ter or the Canadian National Data Center (CNDC). This re-
1022 search was supported by a contract from the US Department
1023 of Energy, DE-FC52-2005NA26607, and two grants from the
1024 US National Science Foundation, EAR-0450082 and EAR-
1025 0408228 (GEON project support for Bensen).

References

- 1026 Alsina, D., R. L. Woodward, and R. K. Snieder (1996), Shear
1027 wave velocity structure in North America from large-scale
1028 waveform inversions of surface waves, *J. Geophys. Res.*,
1029 *101*(B7), 15,969–15,986.
- 1030 Barmin, M. P., M. H. Ritzwoller, and A. L. Levshin (2001),
1031 A fast and reliable method for surface wave tomography,
1032 *Pure Appl. Geophys.*, *158*(8), 1351–1375.
- 1033 Bensen, G. D., M. H. Ritzwoller, M. P. Barmin, A. L. Lev-
1034 shin, F. Lin, M. P. Moschetti, N. M. Shapiro, and Y. Yang
1035 (2007), Processing seismic ambient noise data to obtain re-
1036 liable broad-band surface wave dispersion measurements,
1037 *Geophys. J. Int.*, (169), 1239–1260.
- 1038 Butler, R., et al. (2004), The Global Seismographic Network
1039 surpasses its design goal, *EOS Transactions*, *85*(23), 225–
1040 229.

- 1041 Campillo, M., and A. Paul (2003), Long-range correlations in
1042 the diffuse seismic coda, *Science*, *299*(5606), 547–549.
- 1043 Cho, K. H., R. B. Herrmann, C. J. Ammon, and K. Lee
1044 (2007), Imaging the upper crust of the Korean Peninsula
1045 by surface-wave tomography, *Bull. Seis. Soc. Am.*, *97*(1B),
1046 198–207.
- 1047 Derode, A., E. Larose, M. Campillo, and M. Fink (2003), How
1048 to estimate the Green's function of a heterogeneous medium
1049 between two passive sensors? Application to acoustic
1050 waves, *Appl. Phys. Lett.*, *83*(15), 3054–3056.
- 1051 Ekström, G., J. Tromp, and E. W. F. Larson (1997), Mea-
1052 surements and global models of surface wave propagation,
1053 *J. Geophys. Res.*, *102*(B4), 8137–8157.
- 1054 Gerstoft, P., K. Sabra, P. Roux, W. Kuperman, and M. Fehler
1055 (2006), Greens functions extraction and surface-wave to-
1056 mography from microseisms in southern California, *Geo-
1057 physics*, *71*(4), 23–31.
- 1058 Godey, S., R. Snieder, A. Villaseñor, and H. M. Benz
1059 (2003), Surface wave tomography of North America and
1060 the Caribbean using global and regional broad-band net-
1061 works: phase velocity maps and limitations of ray theory,
1062 *Geophys. J. Int.*, *152*(3), 620–632.
- 1063 Larose, E., A. Derode, M. Campillo, and M. Fink (2004),
1064 Imaging from one-bit correlations of wideband diffuse wave
1065 fields, *J. Appl. Phys.*, *95*(12), 8393–8399.
- 1066 Larose, E., A. Derode, D. Clorennec, L. Margerin, and
1067 M. Campillo (2005), Passive retrieval of Rayleigh waves in
1068 disordered elastic media, *Phys. Rev. E*, *72*(4), 046,607(8),
1069 doi:10.1103/PhysRevE.72.046607.
- 1070 Laske, G., and G. Masters (1997), A global digital map of
1071 sediment thickness, *EOS Trans. AGU*, *78*, 483.
- 1072 Levshin, A. L., V. F. Pisarenko, and G. A. Pogrebinsky (1972),
1073 On a frequency-time analysis of oscillations, *Ann. Geo-
1074 phys.*, *28*(2), 211–218.
- 1075 Lin, F., M. P. Moschetti, and M. H. Ritzwoller (2007a), Sur-
1076 face wave tomography of the western United States from
1077 ambient seismic noise: Rayleigh and Love wave phase ve-
1078 locity maps, *Geophys. J. Int.*, submitted.
- 1079 Lin, F., M. H. Ritzwoller, J. Townend, M. Savage, and S. Ban-
1080 nister (2007b), Ambient noise Rayleigh wave tomography of
1081 New Zealand, *Geophys. J. Int.*, *170*(2), doi:10.1111/j.1365-
1082 246X.2007.03414.x.
- 1083 Lobkis, O. I., and R. L. Weaver (2001), On the emergence of
1084 the Greens function in the correlations of a diffuse field, *J.
1085 Acous. Soc. Am.*, *110*(6), 3011–3017.
- 1086 Moschetti, M. P., M. H. Ritzwoller, and N. M. Shapiro (2007),
1087 Surface wave tomography of the western United States
1088 from ambient seismic noise: Rayleigh wave group veloc-
1089 ity maps, *Geochem. Geophys. Geosys.*, *8*(Q08010), doi:
1090 10.1029/2007GC001655.
- 1091 Ritzwoller, M. H., and A. L. Levshin (1998), Eurasian sur-
1092 face wave tomography - group velocities, *J. Geophys. Res.*,
1093 *103*(B3), 4839–4878.
- 1094 Ritzwoller, M. H., N. M. Shapiro, M. P. Barmin, and
1095 A. L. Levshin (2002), Global surface wave diffraction to-
1096 mography, *J. Geophys. Res.*, *107*(B12), 2335–2347, doi:
1097 10.1029/2002JB001777.
- 1098 Sabra, K. G., P. Gerstoft, P. Roux, W. Kuperman, and
1099 M. C. Fehler (2005), Surface wave tomography from micro-
1100 seisms in Southern California, *Geophys. Res. Lett.*, *32*(14),
1101 14,311–14,314.
- 1102 Seber, D., M. Vallvé, E. Sandvol, D. Steer, and M. Barazangi
1103 (1997), Middle East tectonics: Applications of Geographic
1104 Information Systems (GIS), *GSA Today*, *7*(2), 1–6.
- 1105 Shapiro, N. M., and M. Campillo (2004), Emergence of broad-
1106 band Rayleigh waves from correlations of the ambient seis-
1107 mic noise, *Geophys. Res. Lett.*, *31*(7), 7614–7617.
- 1108 Shapiro, N. M., and M. H. Ritzwoller (2002), Monte-Carlo
1109 inversion for a global shear-velocity model of the crust and
1110 upper mantle, *Geophys. J. Int.*, *151*(1), 88–105.
- 1111 Shapiro, N. M., M. Campillo, L. Stehly, and M. H. Ritzwoller
1112 (2005), High-resolution surface-wave tomography from am-
1113 bient seismic noise, *Science*, *307*(5715), 1615–1618.
- 1114 Snieder, R. K. (2004), Extracting the Greens function from the
1115 correlation of coda waves: A derivation based on stationary
1116 phase, *Phys. Rev. E*, *69*(4), 046,610(8).

- 1117 Spetzler, J., J. Trampert, and R. K. Snieder (2002), The effect
1118 of scattering in surface wave tomography, *Geophys. J. Int.*,
1119 *149*(3), 755–767.
- 1120 Stehly, L., M. Campillo, and N. M. Shapiro (2006), A study of
1121 the seismic noise from its long-range correlation properties,
1122 *J. Geophys. Res.*, *111*(B10), doi:10.1029/2005JB004237.
- 1123 Stehly, L., M. Campillo, and N. M. Shapiro (2007), Traveltime
1124 measurements from noise correlation: stability and detec-
1125 tion of instrumental time-shifts, *Geophys. J. Int.*, *171*(1),
1126 doi:10.1111/j.1365-246X.2007.03492.x.
- 1127 Tanimoto, T., and K. P. Sheldrake (2002), Three-dimensional
1128 S-wave velocity structure in Southern California, *Geophys.*
1129 *Res. Lett.*, *29*(8), 64–68.
- 1130 Trampert, J., and J. H. Woodhouse (1996), High resolution
1131 global phase velocity distributions, *Geophys. Res. Lett.*,
1132 *23*(1), 21–24.
- 1133 van der Lee, S., and G. Nolet (1997), Upper mantle S velocity
1134 structure of North America, *J. Geophys. Res.*, *102*(B10),
1135 22,815–22,838.
- 1136 Villaseñor, A., Y. Yang, M. H. Ritzwoller, and J. Gallart
1137 (2007), Ambient noise surface wave tomography of the
1138 Iberian Peninsula: Implications for shallow seismic struc-
1139 ture, *Geophys. Res. Lett.*, *34*, doi:10.1029/2007GL030164.
- 1140 Wapenaar, K. (2004), Retrieving the elastodynamic Green’s
1141 function of an arbitrary inhomogeneous medium by cross
1142 correlation, *Phys. Rev. Lett.*, *93*(25), 254,301(4), doi:
1143 10.1103/PhysRevLett.93.254301.
- 1144 Weaver, R. L., and O. I. Lobkis (2001), Ultrasonics with-
1145 out a source: Thermal fluctuation correlations at MHz
1146 frequencies, *Phys. Rev. Lett.*, *87*(13), 134,301(4), doi:
1147 10.1103/PhysRevLett.87.134301.
- 1148 Yang, Y., and M. H. Ritzwoller (2007), The characteristics of
1149 ambient seismic noise as a source for surface wave tomog-
1150 raphy, *Geochem. Geophys. Geosys.*, submitted.
- 1151 Yang, Y., M. H. Ritzwoller, A. L. Levshin, and N. M. Shapiro
1152 (2007), Ambient noise Rayleigh wave tomography across
1153 Europe, *Geophys. J. Int.*, *168*(1), 259–274.
- 1154 Yao, H., R. D. van der Hilst, and M. V. de Hoop (2006),
1155 Surface-wave array tomography in SE Tibet from ambi-
1156 ent seismic noise and two-station analysis-I. Phase velocity
1157 maps, *Geophys. J. Int.*, *166*(2), 732–744.
- 1158 Yoshizawa, K., and B. L. N. Kennett (2002), Determination
1159 of the influence zone for surface wave paths, *Geophys. J.*
1160 *Int.*, *149*(2), 440–453.

1161 G. D. Bensen, Department of Physics, University of Col-
1162 orado at Boulder, Campus Box 390, Boulder, CO 80309, USA.
1163 (gbensen@colorado.edu)

Table 1. Number of Rayleigh wave measurements rejected and selected prior to tomography at 10-, 16-, 25-, 50-, and 70-s periods.

<i>Period</i>	10-s	16-s	25-s	50-s	70-s
Total waveforms	18554	18554	18554	18554	18554
Distance rejections	487	933	1608	3465	4818
SNR < 10	7416	5049	5327	9990	10686
<i>Group velocity rejections</i>					
Stdev > 100 m/s or undefined	3348	3418	3624	2782	1799
3 σ time residual rejection	182	222	104	32	29
Remaining group measurements	7121	8932	7891	2285	1222
<i>Phase velocity rejections</i>					
Stdev > 100 m/s or undefined	3296	3561	3603	1626	941
3 σ time residual rejection	161	321	135	58	36
Remaining phase measurements	7194	8690	7881	3415	2073

Table 2. Same as Table 1 but for Love waves.

<i>Period</i>	10-s	16-s	25-s
Total waveforms	18554	18554	18554
Distance rejections	487	933	1608
SNR < 10	8690	7042	13591
<i>Group velocity rejections</i>			
Stdev > 100 m/s or undefined	2709	2563	1324
3 σ time residual rejection	222	245	63
Remaining group measurements	6446	7771	1968
<i>Phase velocity rejections</i>			
Stdev > 100 m/s or undefined	2848	4332	1266
3 σ time residual rejection	200	166	94
Remaining phase measurements	6329	6081	1995

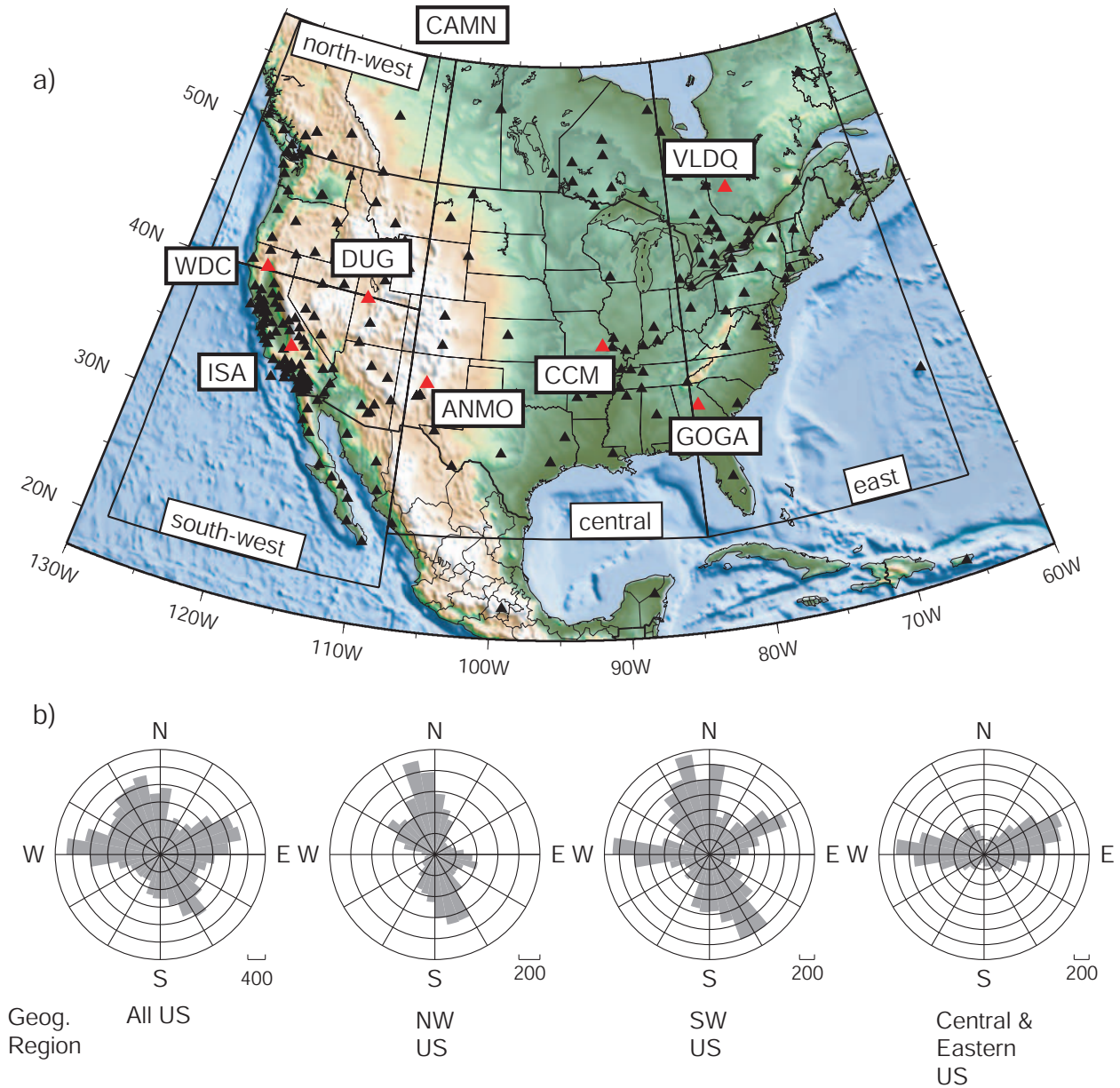


Figure 1. (a) The study area with stations represented as triangles. Red triangles with station names indicate inter-station paths for the waveforms and dispersion curves in Fig. 2. The study area is divided into four boxed sub-regions. (b) Azimuthal distribution of inter-station paths, plotted as the number of paths per 10° azimuthal bin, for the entire data set (at left) and in several sub-regions. Both azimuth and back-azimuth are included and indicate the direction of propagation of waves. Station CAMN is just north of the map boundary at $63.76, -110.89$.

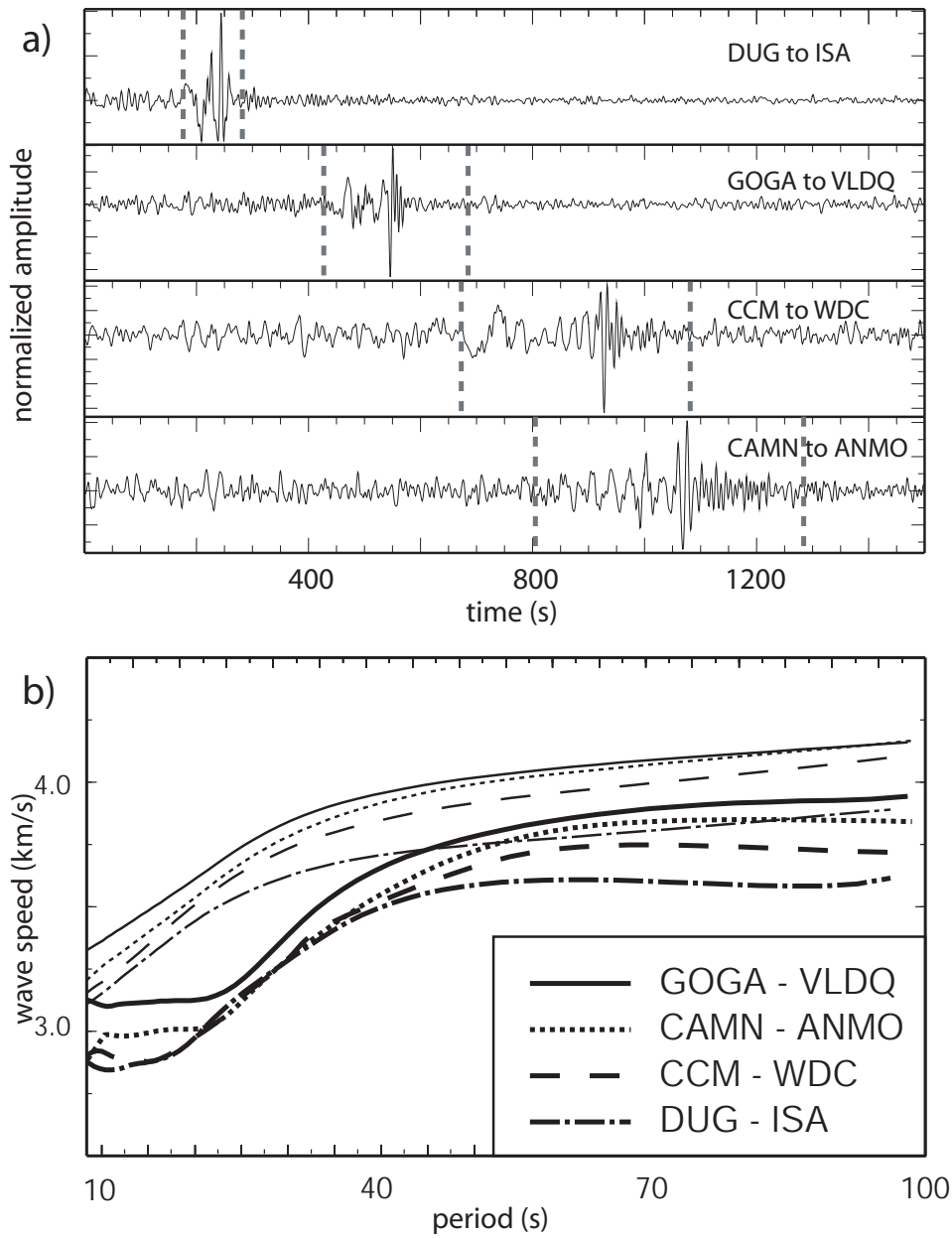


Figure 2. (a) Examples of broad-band vertical-component symmetric signal empirical Green functions (Rayleigh waves) through various tectonic regimes for the inter-station paths indicated with red triangles in Fig. 1a. Waveforms are filtered between 7 and 100 s period. The time windows marked with vertical dashed lines are at 2.5 and 4.0 km/s. (b) The corresponding measured group and phase speed curves. Group velocity curves are thicker than phase velocity curves.

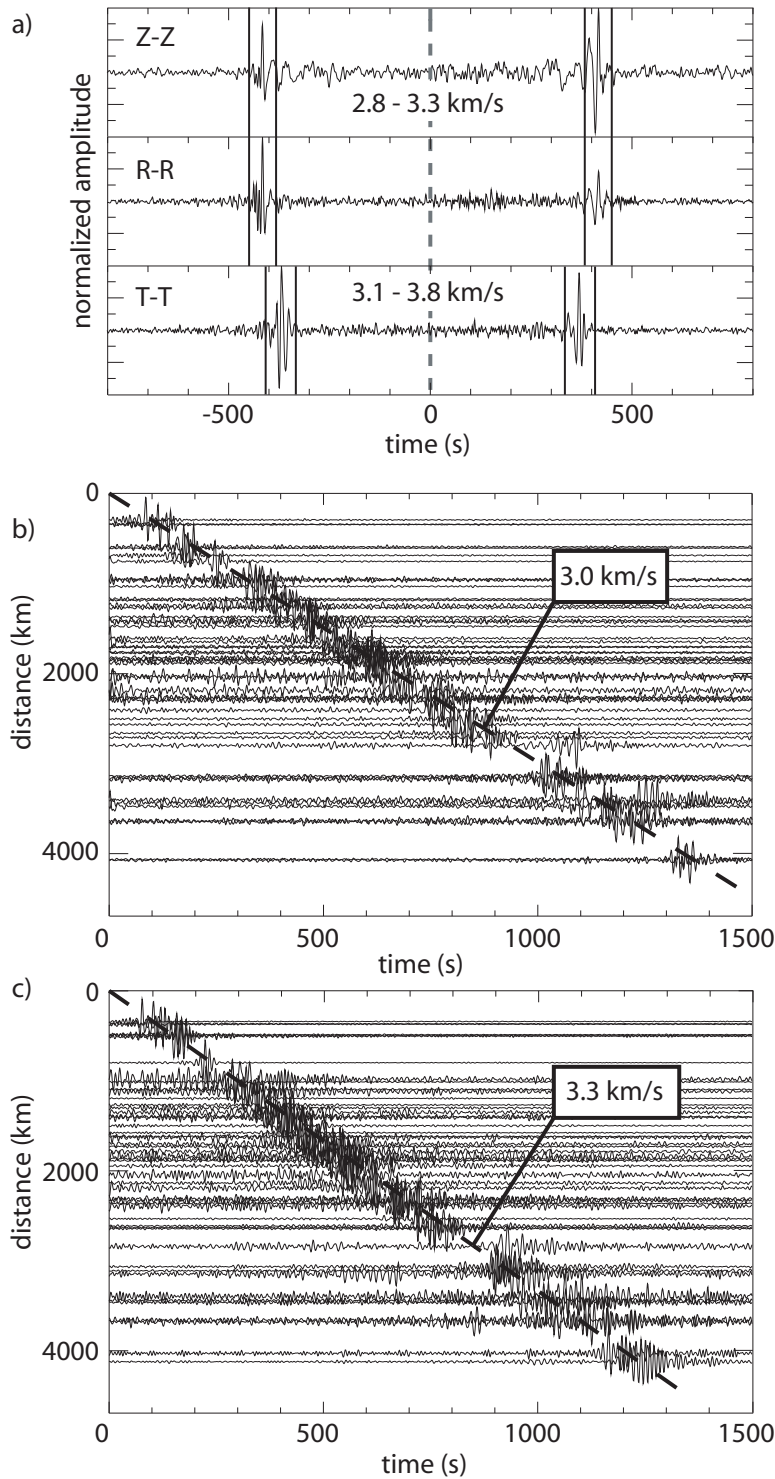


Figure 3. Example Rayleigh and Love wave empirical Green functions (EGFs). (a) Two-sided EGFs filtered between 5 and 50 s period for the stations CCM and RSSD. Rayleigh wave signals emerge on the Z-Z and R-R empirical Green functions (EGFs) and are highlighted with a velocity window from 2.8 - 3.3 km/s. Love waves are seen on the T-T component, identified with an arrival window from 3.1 - 3.8 km/s. (b) Record section containing all EGFs between Z-Z components from GSN stations in the US separated by the specified inter-station distance. (c) Same as (b), but for the T-T component. Move-outs of 3.0 and 3.3 km/s are indicated in (b) and (c), respectively.

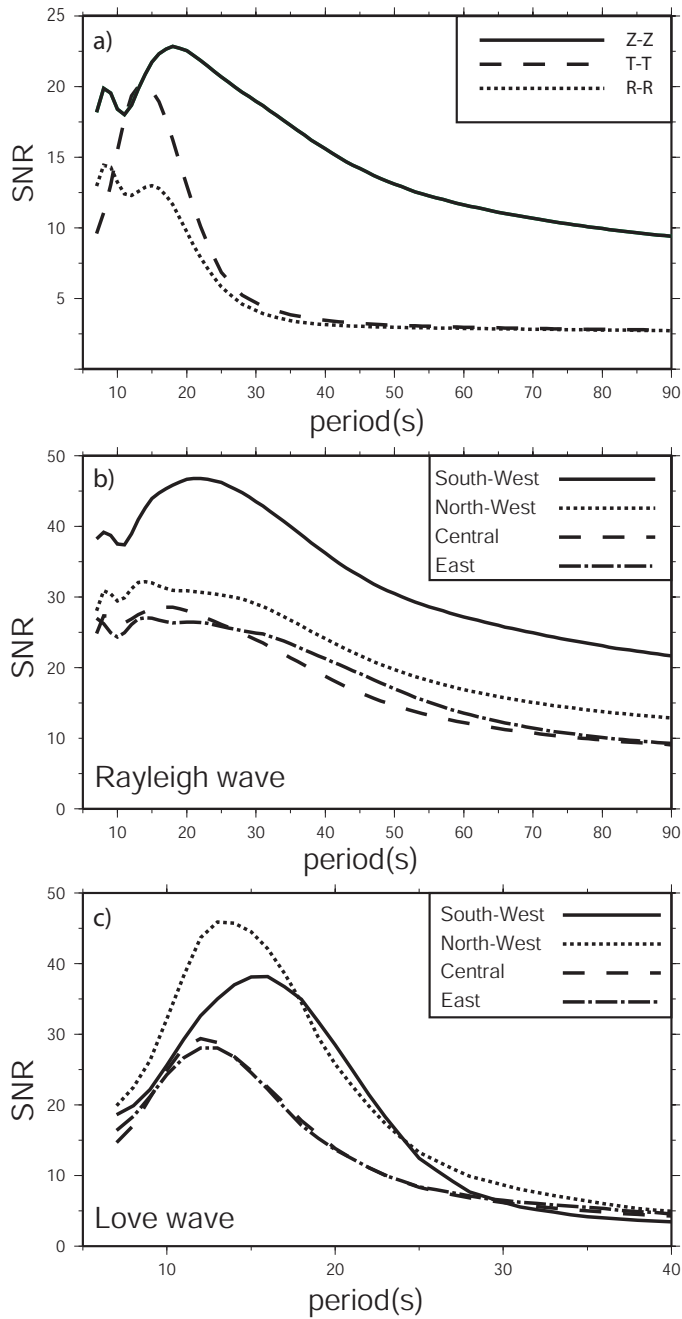


Figure 4. (a)Relative signal quality represented as the average signal-to-noise ratio (SNR) for Rayleigh and Love waves computed using all stations in the study region. Rayleigh waves appear on vertical-vertical (Z-Z) and radial-radial (R-R) components, while Love waves are on the transverse-transverse (T-T) component EGFs. The mean signal-to-noise ratio is plotted versus period for (b) Rayleigh (Z-Z) waves and (c) Love (T-T) waves for the different geographical sub-regions defined in Fig. 1a. Note: the period bands for (b) and (c) differ.

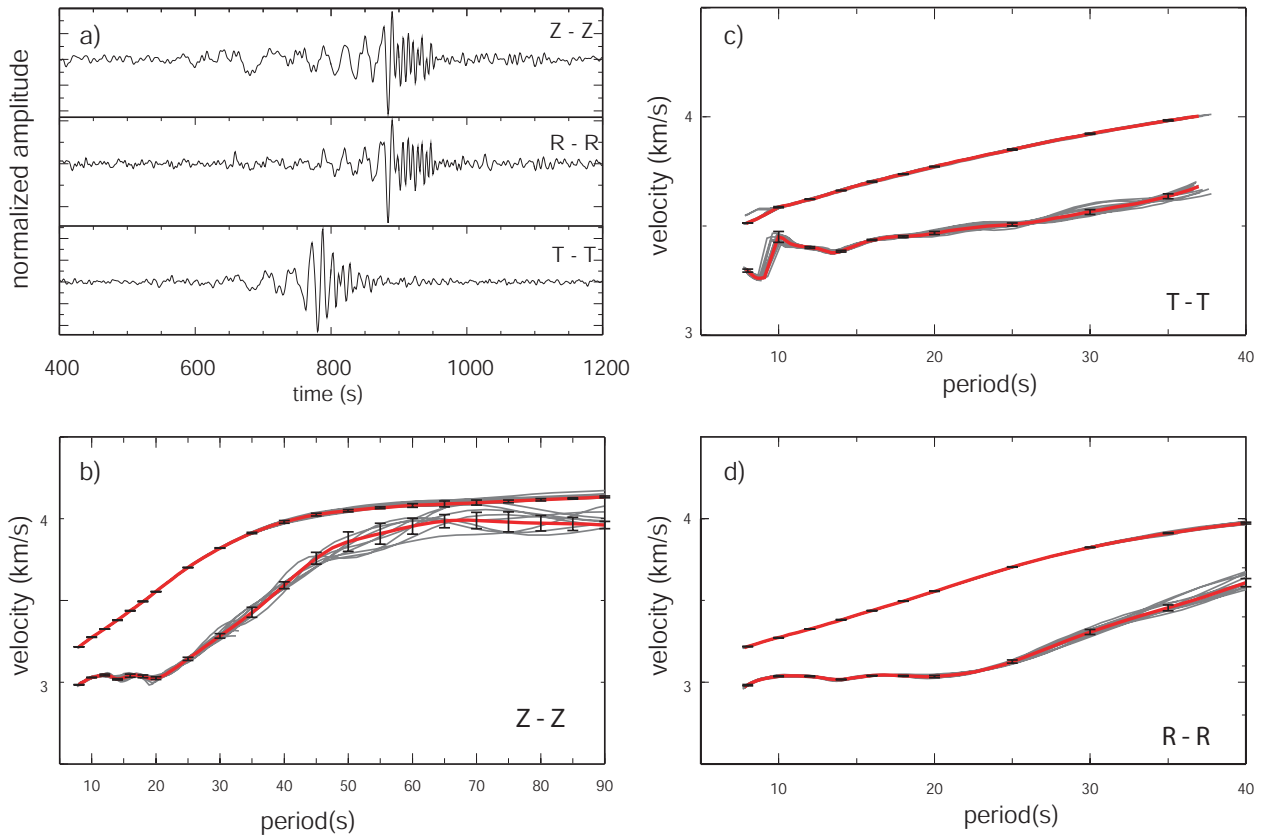


Figure 5. Illustration of the computation of measurement uncertainty. (a) Empirical Green functions (EGFs) on the Z-Z, R-R, and T-T components for the station pair DWPF and RSSD. (b) Measured Rayleigh wave group and phase speed curves from the Z-Z component EGF. The 24-month measurements are plotted in red, individual 6-month measurements are plotted in grey, and the 1- σ error bars summarize the variation among the 6-month results. (c) Same as (b), but for the T-T component (Love waves). (d) Same as (b), but for the R-R component. Note the different period bands and velocity scales in (b)-(d).

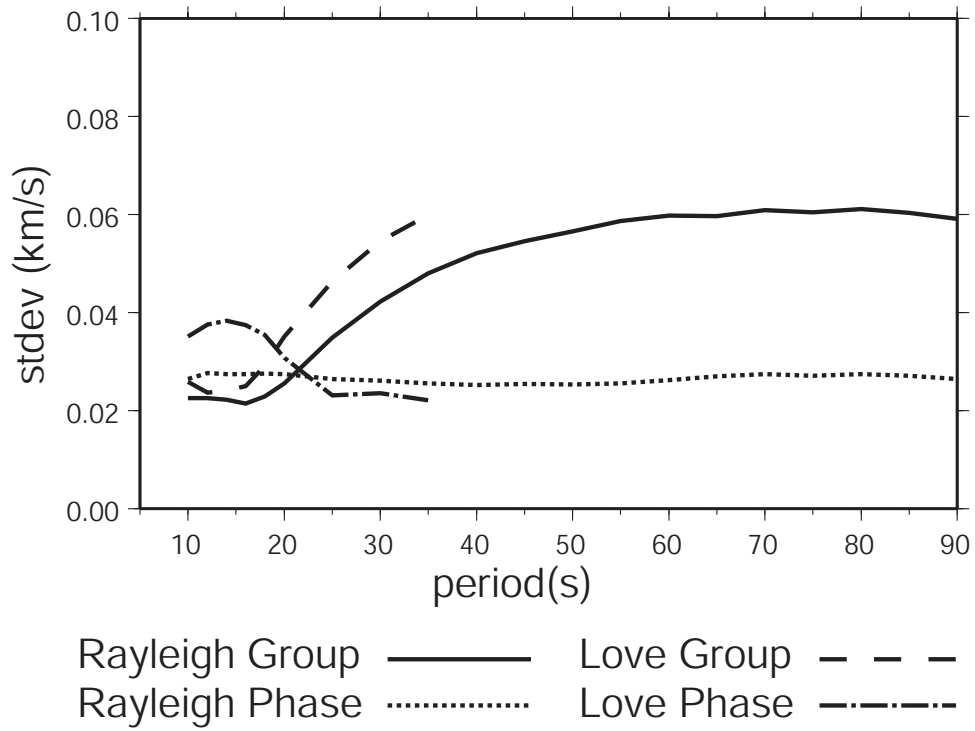


Figure 6. Average dispersion measurement standard deviation versus period for Rayleigh and Love wave group and phase speeds, where the average is taken over all acceptable measurements.

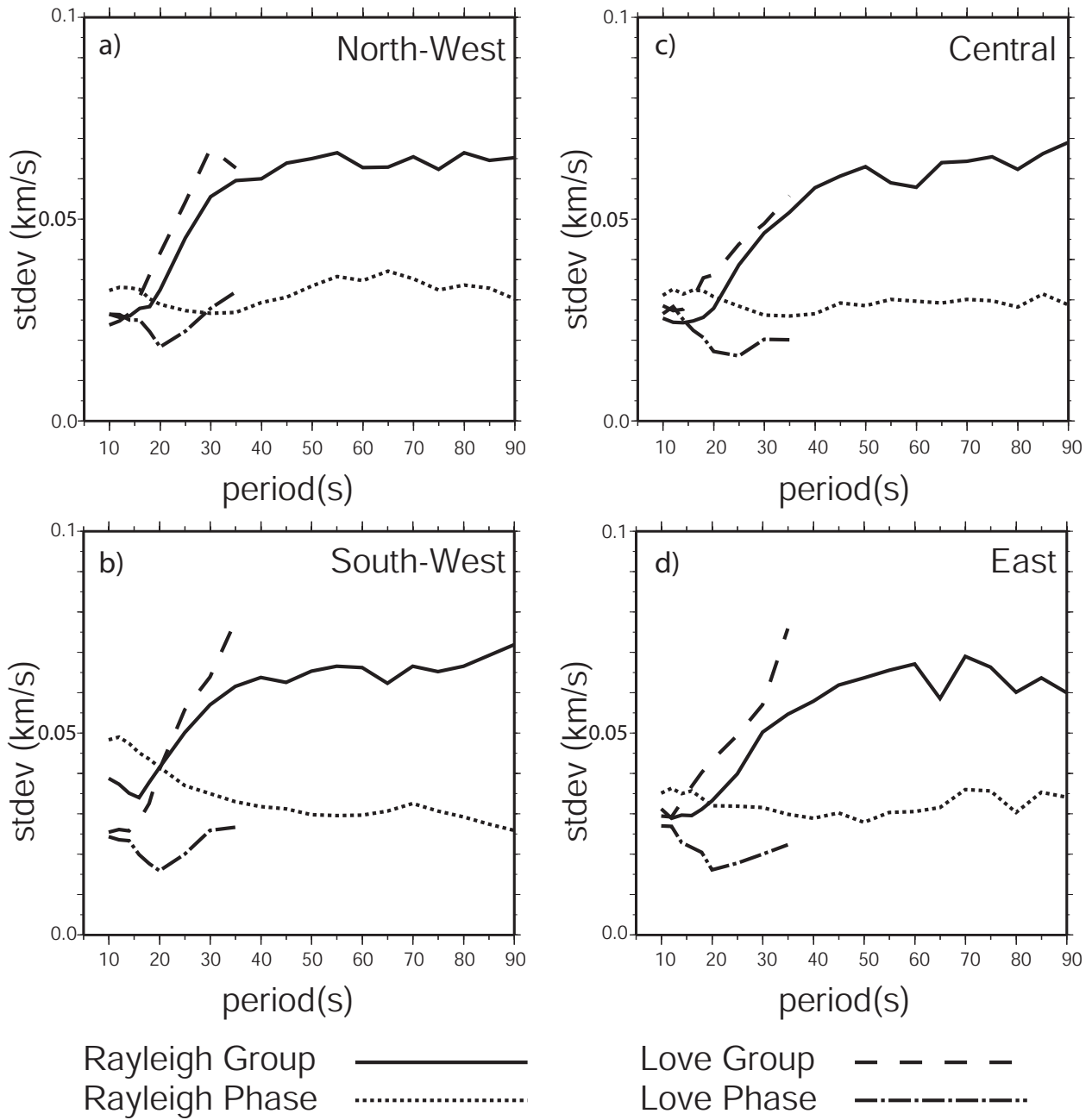


Figure 7. The average standard deviation of the velocity measurements as determined from the 6-month subsets of the data, averaged over all acceptable measurements. (a) - (d) Results are for the four sub-regions defined in Fig. 1a.

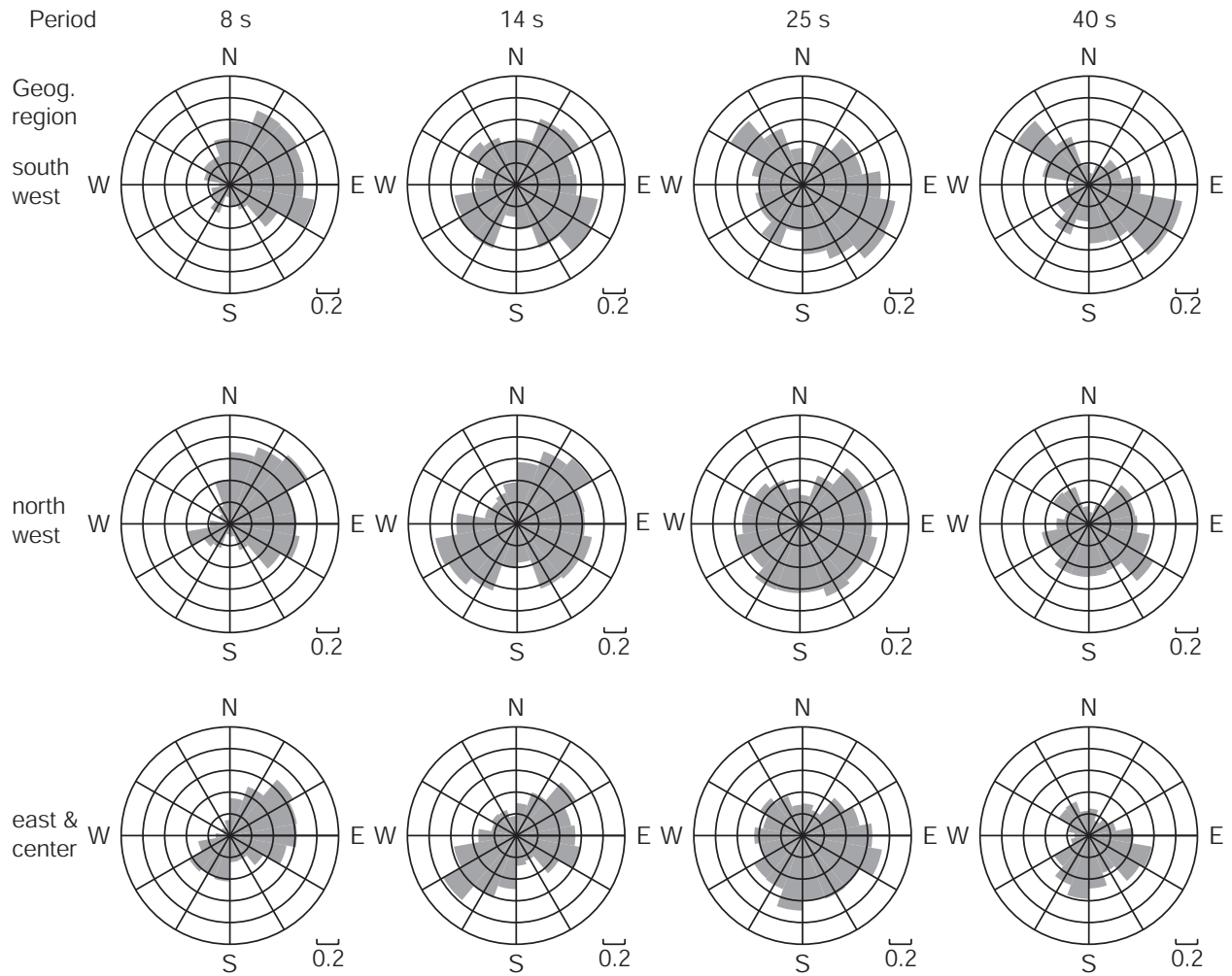


Figure 8. The directional dependence of high SNR (>10) Rayleigh wave EGF signals plotted at different periods (8, 14, 25, 40 s in different columns) and geographical sub-regions (different rows). Azimuth is the direction of propagation of the wave. Results are presented as fractions, in which the numerator is the number of inter-station paths in a particular azimuthal bin with $\text{SNR} > 10$ and the denominator is the number of paths in the bin (from Fig. 1b).

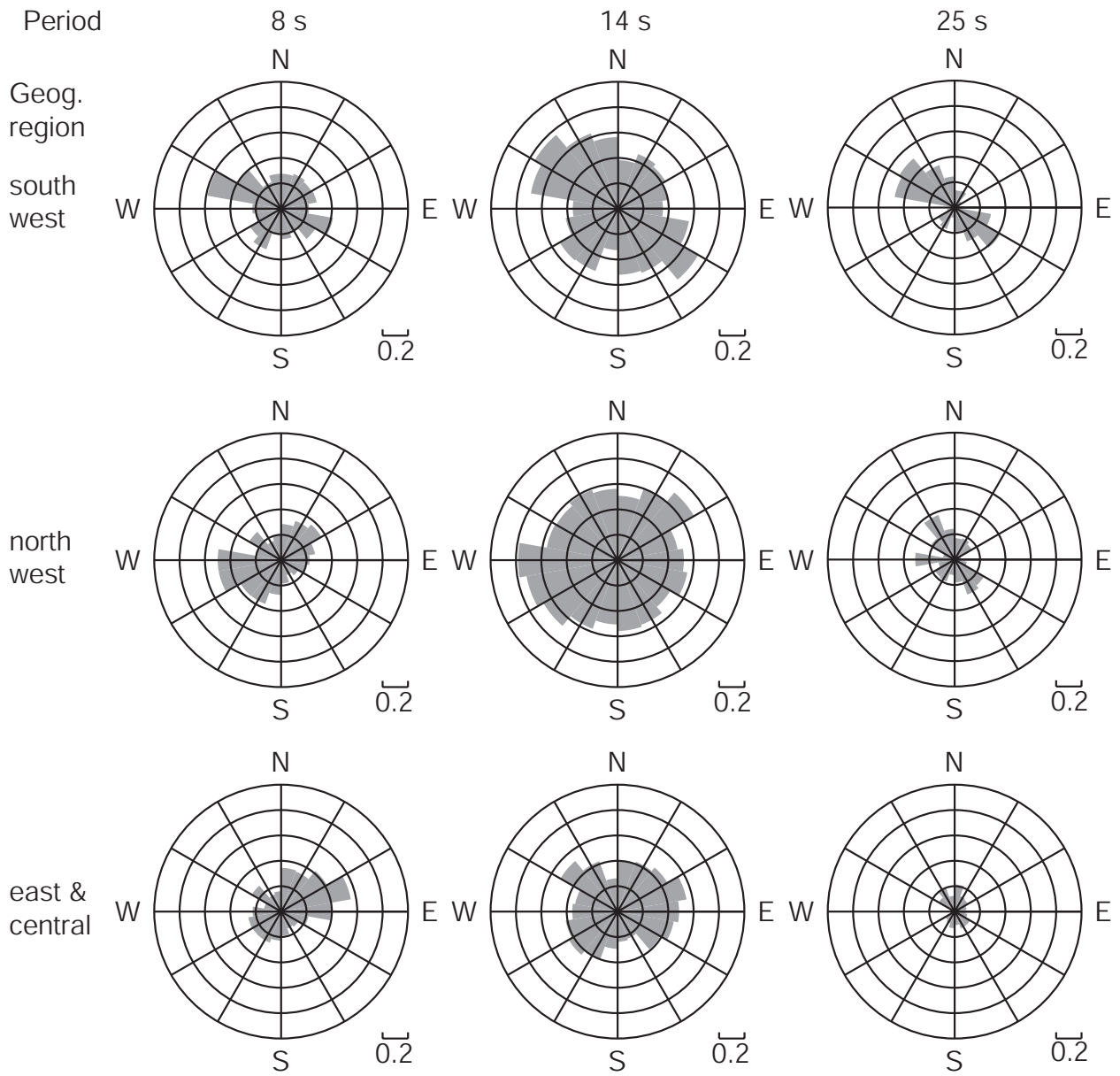


Figure 9. Same as Figure 8, but for Love waves.

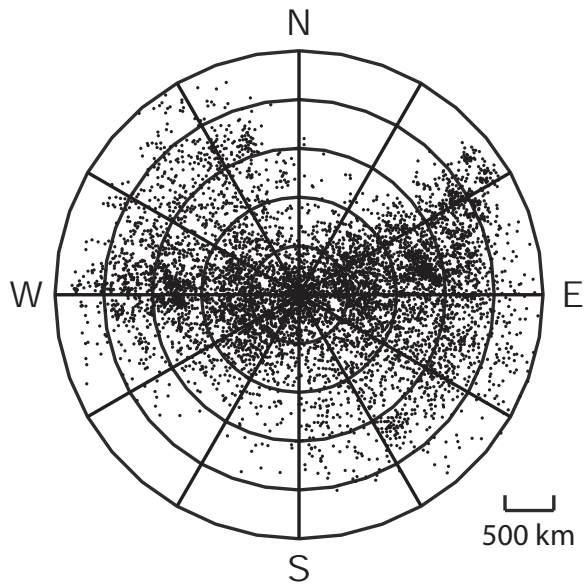


Figure 10. A plot of the azimuth and distance for all signals in the central-east region with $\text{SNR} > 10$ at 25 s period. The sparse regions in the N-NE and S-SW are due to the array configuration.

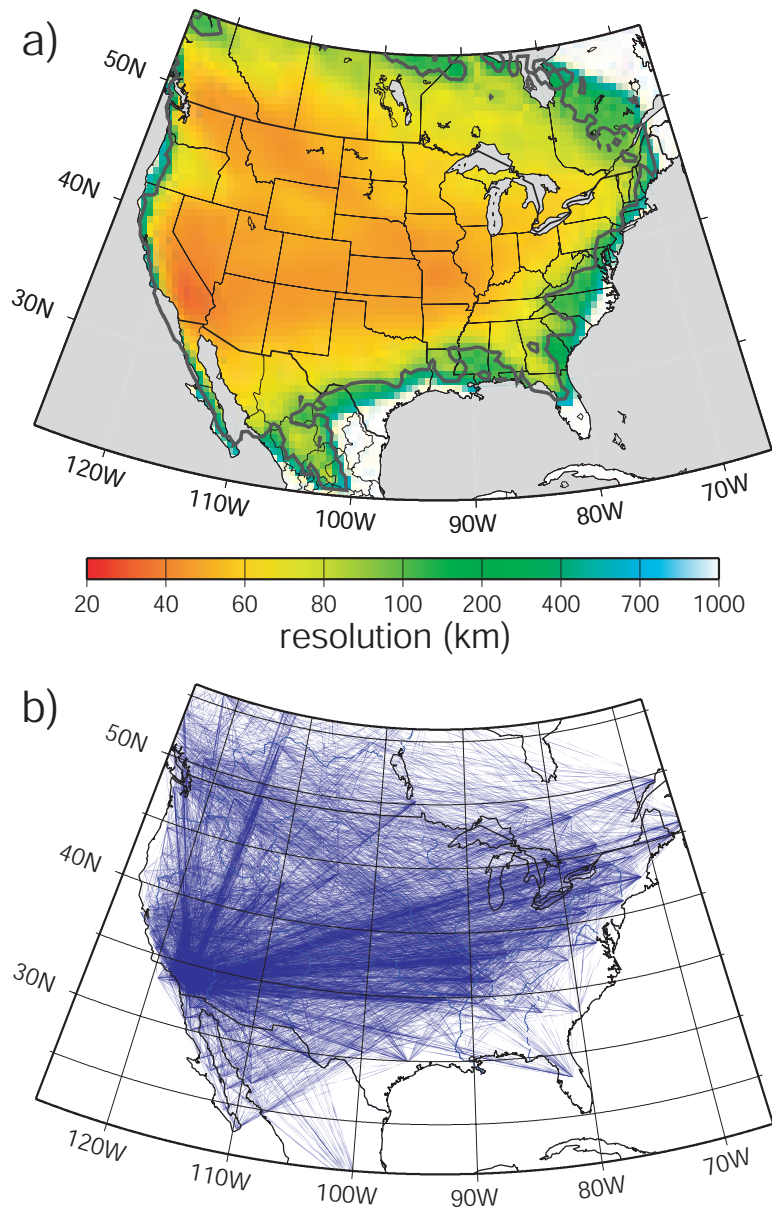


Figure 11. Path distribution and estimated resolution for the 10 s period Rayleigh wave. (a) Resolution is defined as twice the standard deviation (2γ) of the 2-D Gaussian fit to the resolution surface at each point. The 200 km resolution contour is drawn and the color scale saturates at white when the resolution degrades to 1000 km, indicating indeterminate velocities. (b) Paths used to construct (a).

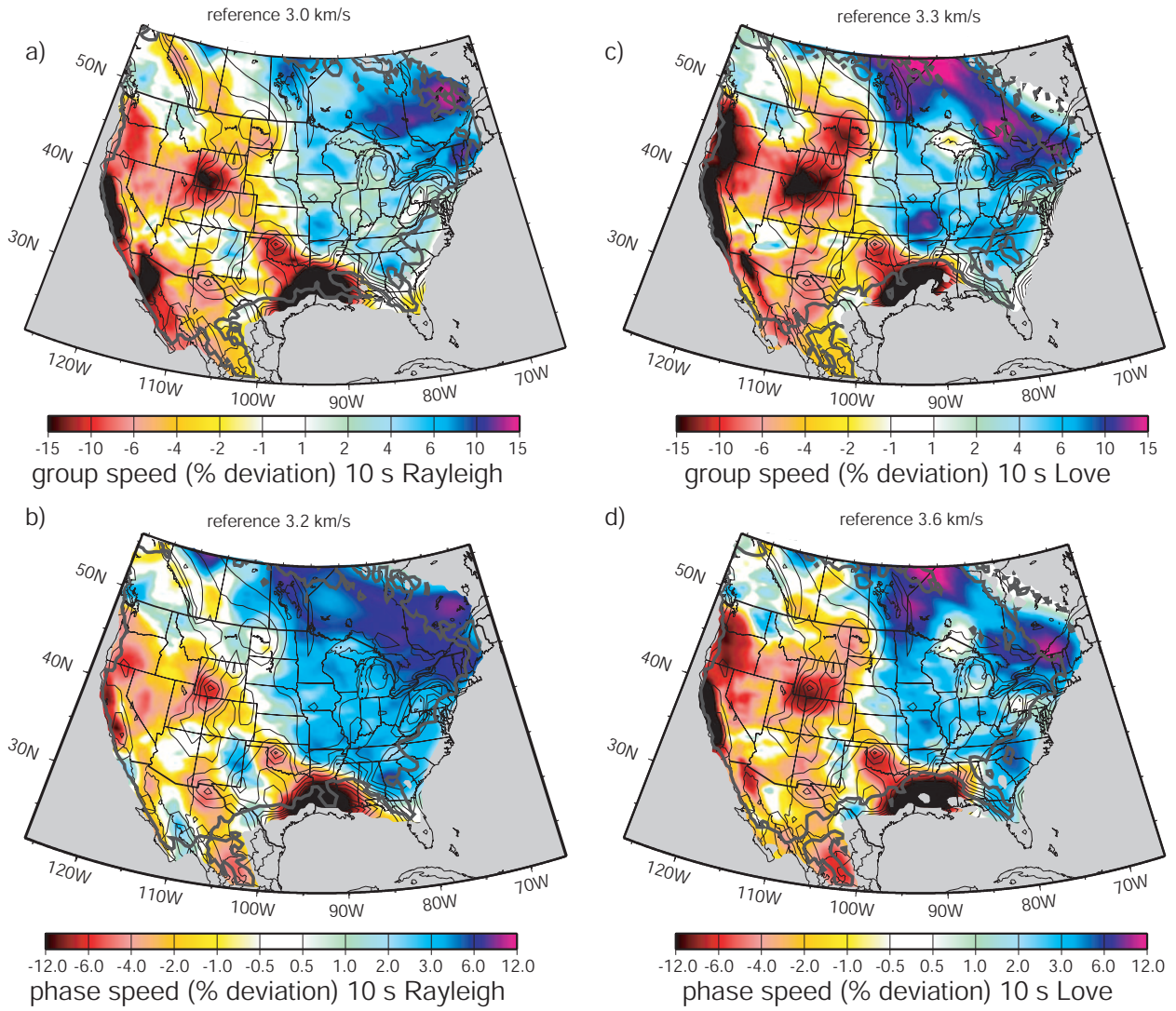


Figure 12. Rayleigh and Love wave group and phase speed dispersion maps at 10 s period: (a) Rayleigh group speed, (b) Rayleigh phase speed, (c) Love group speed, and (d) Love phase speed. The thick grey contour outlines the region with better than 200 km resolution and areas with resolution worse than 1000 km are clipped to grey. Many sedimentary features labeled in Fig. 18 are visible and 1-km contours of the sediment model of *Laske and Masters* [1997] are plotted with thin black lines for reference. Note the differences in reference speeds and color scale ranges.

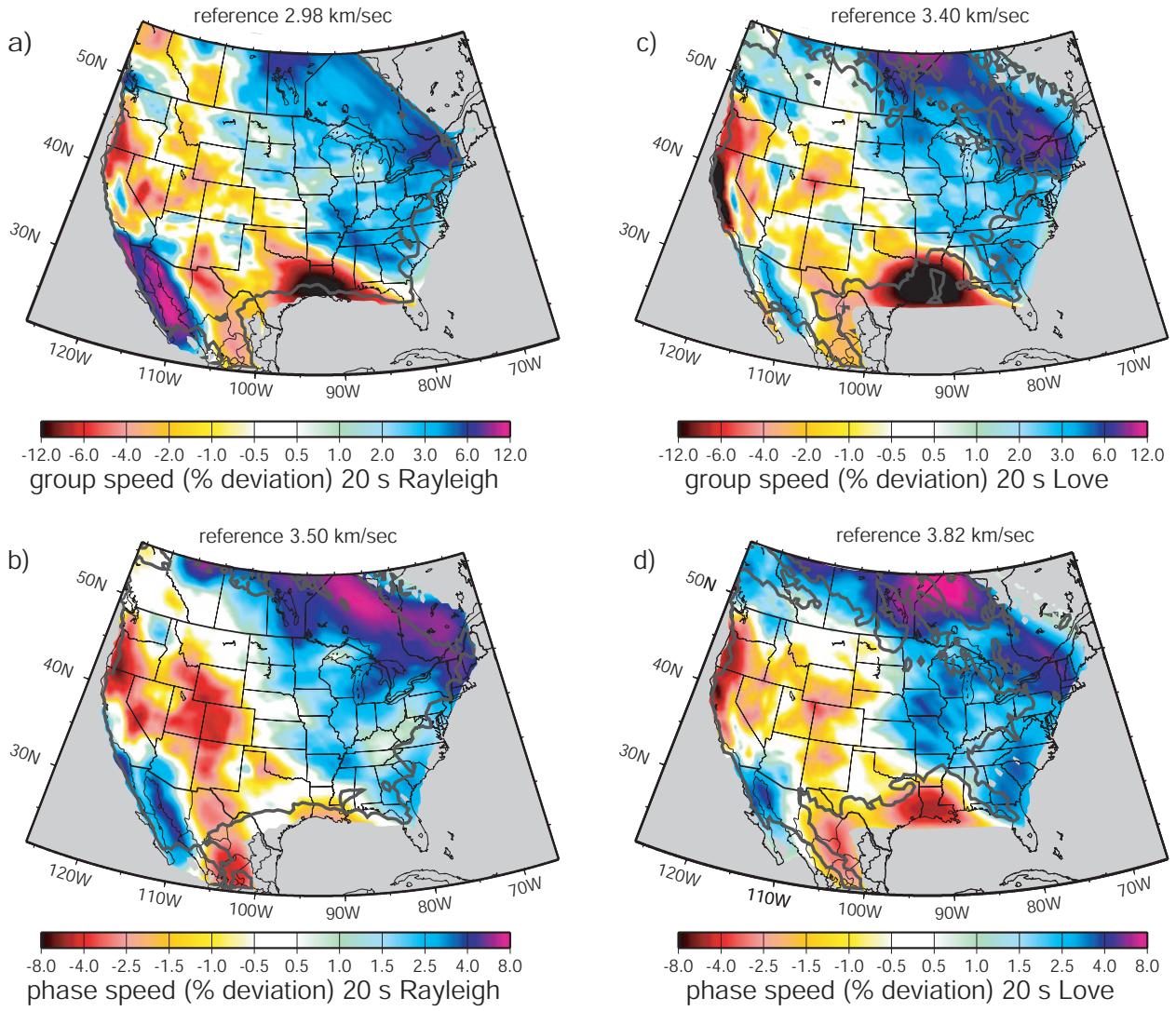


Figure 13. Same as Fig. 12, but for 20 s period and sedimentary contours are suppressed.

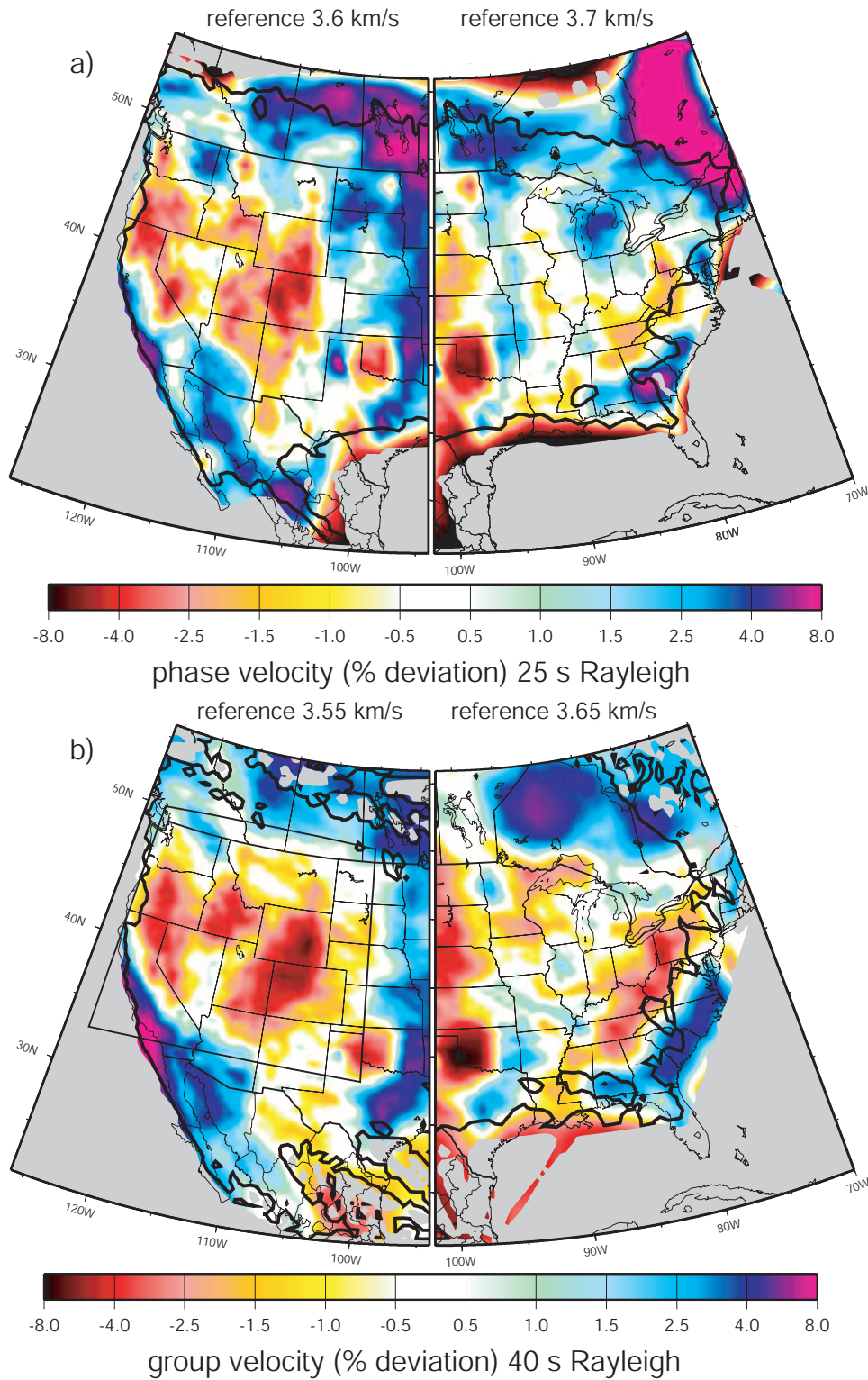


Figure 14. (a) The 25 s period Rayleigh wave phase speed map. (b) The 40 s Rayleigh wave group speed map. Grey contours indicate a resolution of 200 km and resolution less than 1000 km is colored grey. Different reference wave speeds are used in each half of the map and are indicated in the figure. The box in (b) corresponds to the region blown up in Figure 19.

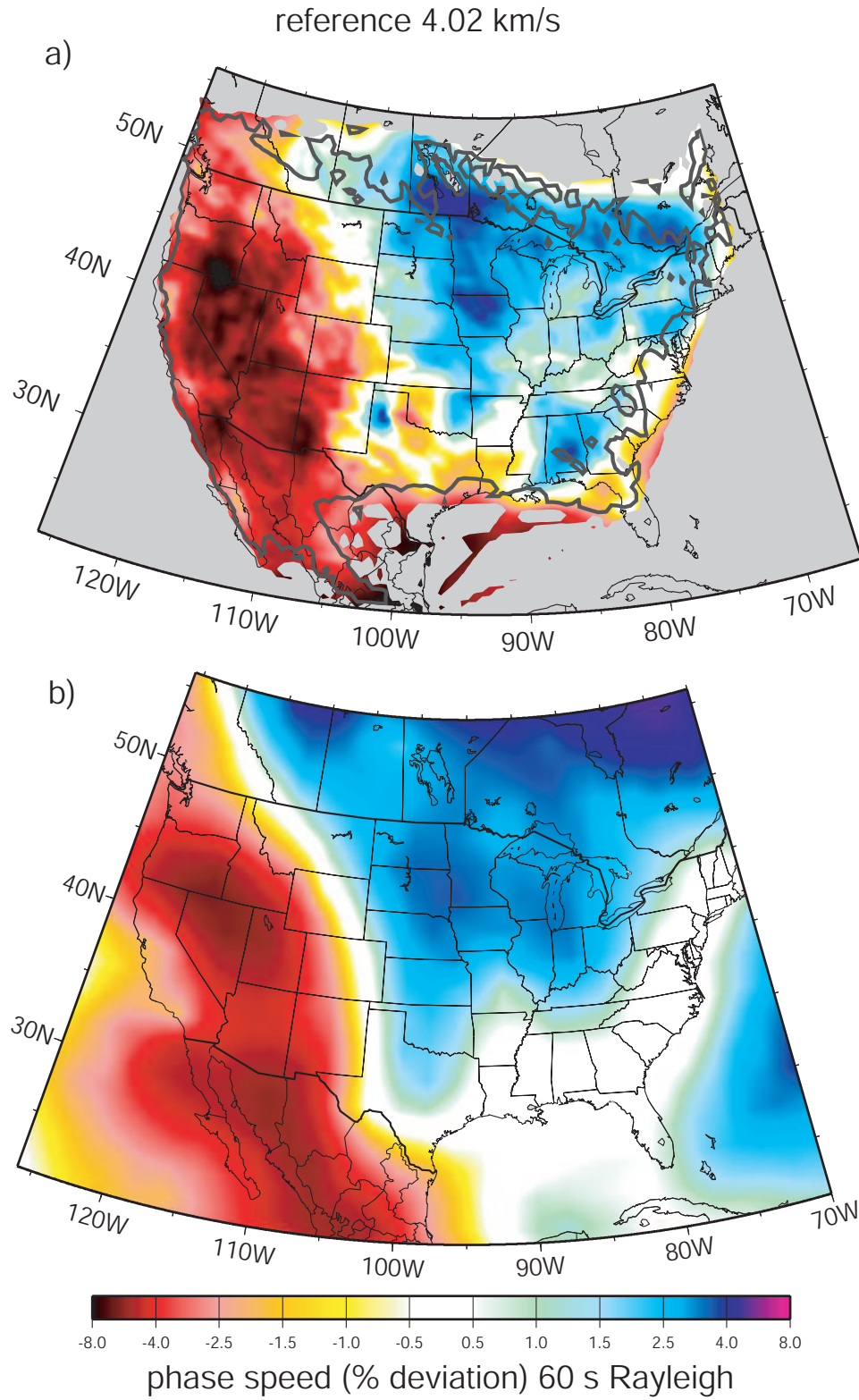


Figure 15. (a) The Rayleigh wave phase speed map at 60 s period. The grey contour outlines the 200 km resolution and continental areas with indeterminate velocity are clipped to white. (b) The prediction from a 3-D global model (*Shapiro and Ritzwoller [2002]*) is shown for comparison.

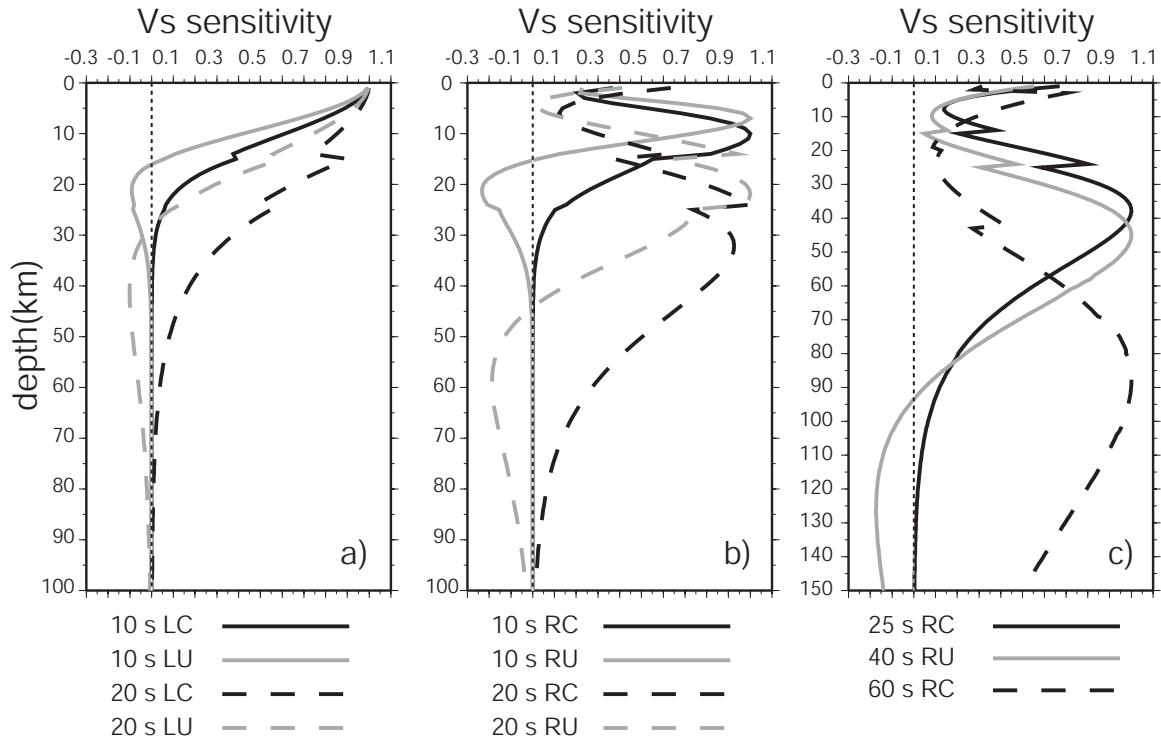


Figure 16. Sensitivity kernels for all dispersion maps shown here. Sensitivities for 10 and 20 s period Love waves are shown in (a), 10 and 20 s period Rayleigh waves are in (b) and longer periods in (c). The kernels have been normalized to have the same maximum amplitude and the labeling is as follows: RC - Rayleigh phase, RU - Rayleigh group, LC - Love phase, LU - Love group. Kernels are computed for PREM but with the ocean replaced by consolidated sediments.

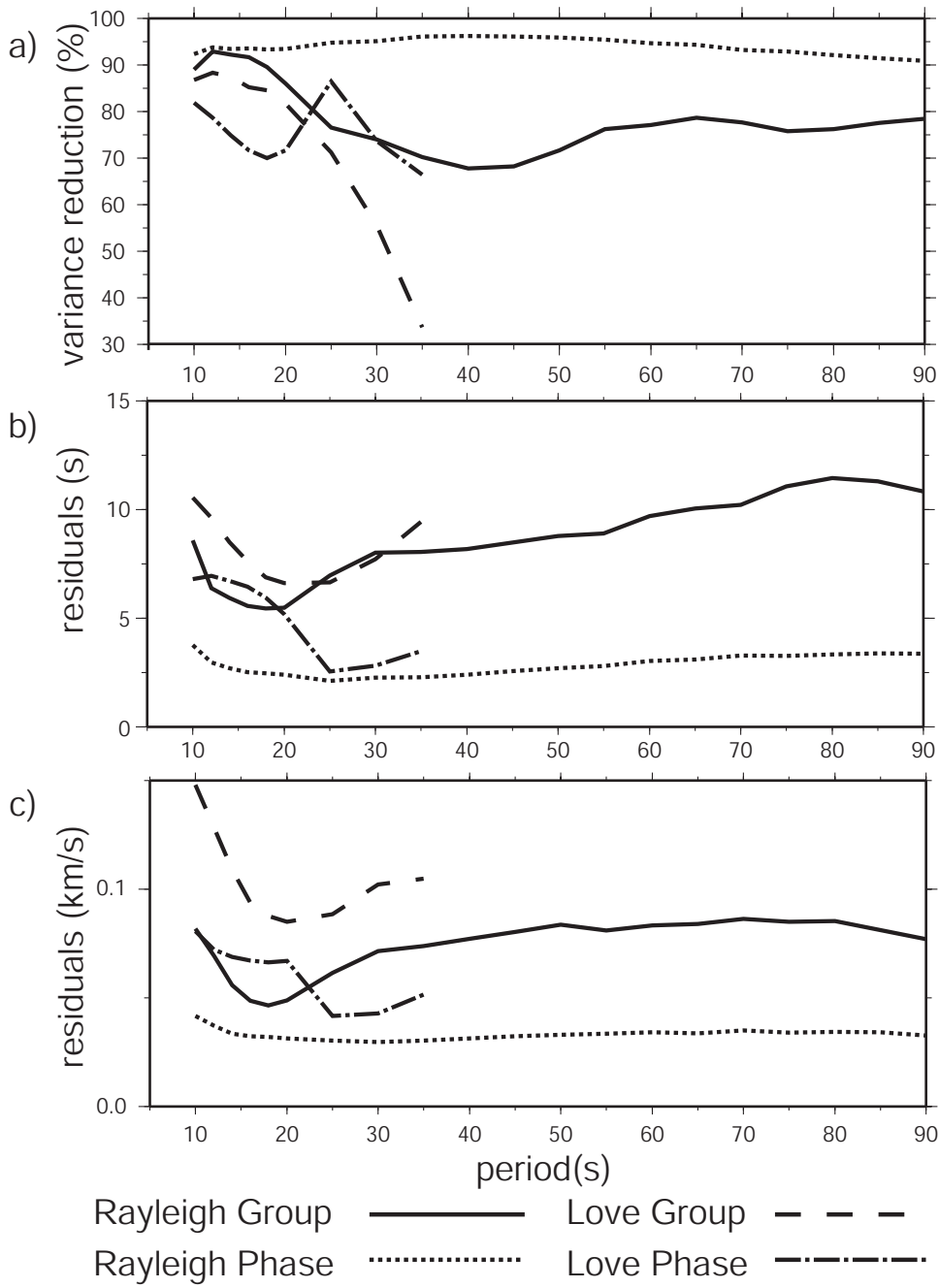


Figure 17. (a) Rayleigh and Love wave group and phase speed variance reduction as a function of period, computed relative to the mean measurement for each wave type and period. (b) The rms final travel-time residuals in s. (c) Final rms velocity residuals.

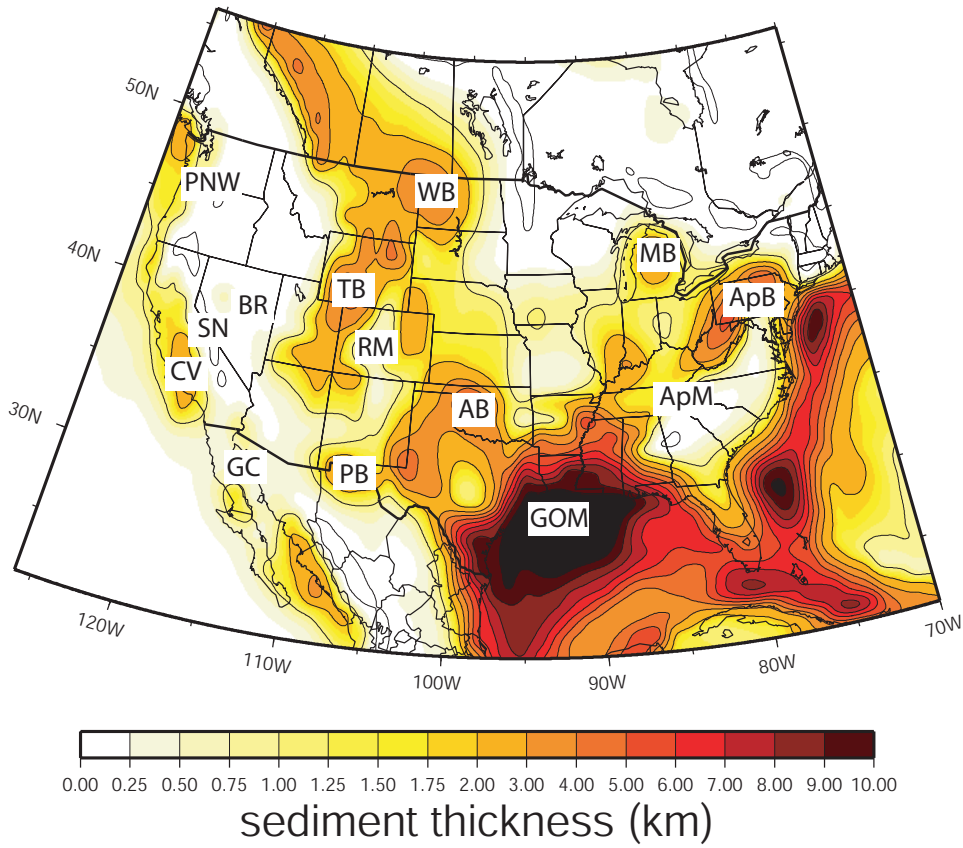


Figure 18. Sediment thickness model of *Laske and Masters* [1997] with several prominent basins and geographical features labeled: ‘CV’ - Central Valley in California, ‘SN’ - Sierra Nevada, ‘AB’ - Anadarko Basin, ‘PB’ - Permian Basin, ‘GOM’ - Gulf of Mexico, ‘TB’- Wyoming-Utah-Idaho thrust belt, ‘WB’ - Williston Basin, ‘ApB’ - Appalachian Basin, ‘MB’ - Michigan Basin, ‘BR’ - Basin and Range, ‘RM’ - Rocky Mountain Region, ‘ApM - Appalachian Mountains’, ‘PNW’ - Pacific Northwest, ‘GC’ - Gulf of California.

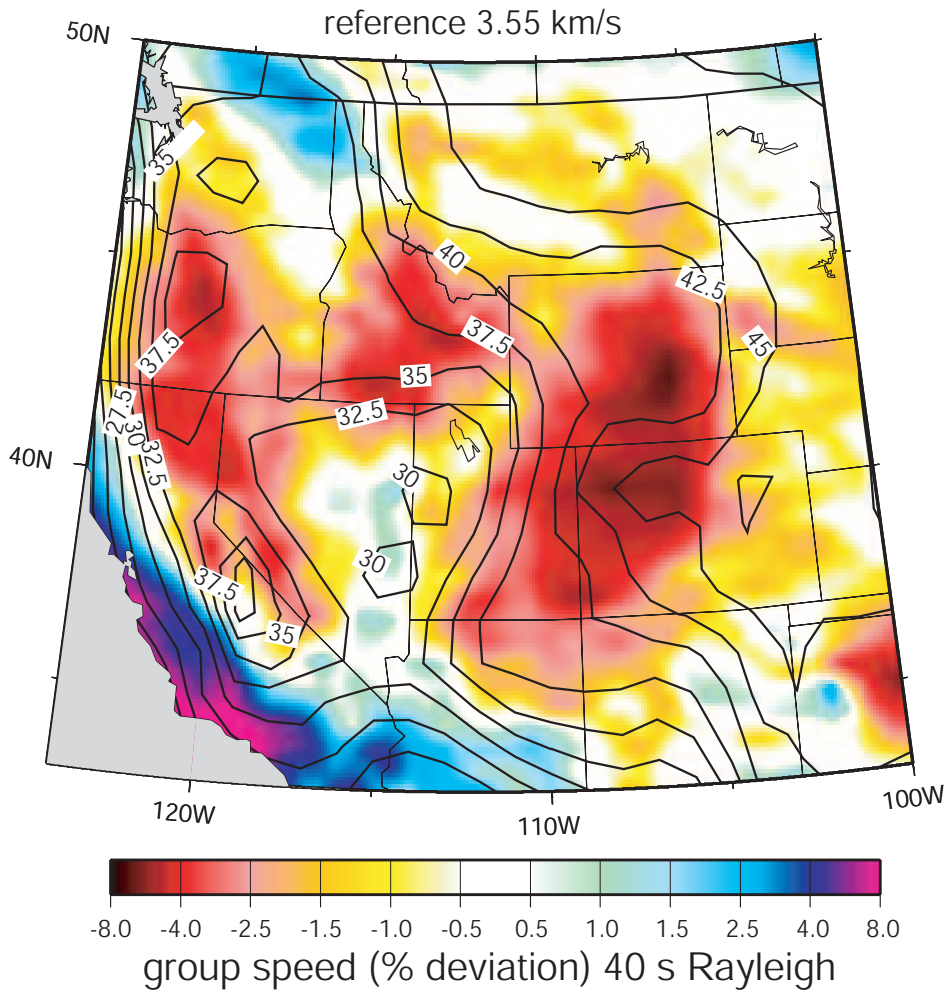


Figure 19. Rayleigh wave group speed dispersion map at 40 s period for the region outlined in Fig. 14b. The Cornell US Moho depth model (*Seber et al.* [1997]) is plotted as contours with a 2.5 km contour interval with a maximum thickness (of 47 km) under Colorado. Low velocities generally correspond to thick crust.